HHS Public Access

Author manuscript

Cell Metab. Author manuscript; available in PMC 2025 January 02.

Published in final edited form as:

Cell Metab. 2024 January 02; 36(1): 62–77.e8. doi:10.1016/j.cmet.2023.11.013.

Myeloid cell-derived creatine in the hypoxic niche promotes glioblastoma growth

Aida Rashidi[1,†], **Leah K. Billingham**[1,†], **Andrew Zolp**[1], **Tzu-yi Chia**[1], **Caylee Silvers**[1], **Joshua L. Katz**[1], **Cheol H. Park**[1], **Suzi Delay**[1], **Lauren Boland**[2], **Yuheng Geng**[1], **Steven M. Markwell**[3], **Crismita Dmello**[1], **Victor A. Arrieta**[1], **Kaylee Zilinger**[1], **Irene M. Jacob**[1], **Aurora Lopez-Rosas**[1], **David Hou**[1], **Brandyn Castro**[1], **Alicia M. Steffens**[1], **Kathleen McCortney**[1], **Jordain P Walshon**[1], **Mariah S. Flowers**[1], **Hanchen Lin**[1], **Hanxiang Wang**[1], **Junfei Zhao**[4], **Adam Sonabend**[1], **Peng Zhang**[1], **Atique U. Ahmed**[1], **Daniel J. Brat**[3], **Dieter H. Heiland**[1,5,6], **Catalina Lee-Chang**[1], **Maciej S. Lesniak**[1], **Navdeep S. Chandel**[7], **Jason Miska**[1,*]

[1]Department of Neurological Surgery, Lou and Jean Malnati Brain Tumor Institute, Feinberg School of Medicine, Northwestern University, 676 N St. Clair, Suite 2210, Chicago, IL 60611, USA

[2]Stanley Manne Children's Research Institute, Ann & Robert H. Lurie Children's Hospital, Chicago, IL, USA

[3]Department of Pathology, Feinberg School of Medicine, Northwestern University, 303 East Chicago Avenue, Chicago, IL 60611, USA

[4]Department of Systems Biology, Columbia University, New York, NY, USA

[5]Microenvironment and Immunology Research Laboratory, Medical Center, University of Freiburg, 79106, Freiburg, Germany

[6]Department of Neurosurgery, Medical Center, University of Freiburg, 79106, Freiburg, Germany. German Cancer Consortium (DKTK), partner site Freiburg, Freiburg, Germany

[*]Lead contact and Corresponding author: Jason Miska, jason.miska@northwestern.edu.
[†]These authors contributed equally

AUTHOR CONTRIBUTIONS

Conceptualization: JM, CLC, NSC, DHH, DJB, AUA, and MSL
Methodology: JM, AZ, AR, CP, LKB, LB, TC, IMJ, PZ, SKM, BC, DH, JLK, CHP, YG, CS, SD, CD, JPW, AMS, KM, MSF, HL, HW,
scRNA-seq analysis: JZ.
Spatial metabolomics and Transcriptomics: DHH
Animal Breeding: ALR
Neuropathologist: DJB
Multiplexed imaging analysis: VAA in conjunction with the Immunotherapy Assessment Core at Northwestern University.
Performed and analyzed LC/MS: PG
Supervision: JM, NSC, MSL, CLC, DJB
Statistical oversight: TX
Writing – original draft: JMM, NSC, AR, AZ, LKB
Writing – review and editing: all authors

DECLARATION OF INTERESTS

Authors declare no competing interests.

[7]Department of Medicine, Feinberg School of Medicine, Northwestern University, 676 North St. Clair Street, Suite 2330, Chicago, IL 60611, USA

SUMMARY

Glioblastoma (GBM) is a malignancy dominated by the infiltration of tumor-associated myeloid cells (TAMCs). Examination of TAMC metabolic phenotypes in mouse models and patients with GBM identified the *de-novo* creatine metabolic pathway as a hallmark of TAMCs. Multi-omics analyses revealed that TAMCs surround the hypoxic peri-necrotic regions of GBM and express the creatine metabolic enzyme glycine amidinotransferase (GATM). Conversely, GBM cells located within these same regions are uniquely specific in expressing the creatine transporter (SLC6A8). We hypothesized that TAMCs provide creatine to tumors, promoting GBM progression. Isotopic tracing demonstrated that TAMC-secreted creatine is taken up by tumor cells. Creatine supplementation protected tumors from hypoxia-induced stress which, was abrogated with genetic ablation or pharmacologic inhibition of SLC6A8. Lastly, inhibition of creatine transport using the clinically relevant compound, RGX-202-01, blunted tumor growth, and enhanced radiation therapy *in-vivo*. This work highlights that myeloid-to-tumor transfer of creatine promotes tumor growth in the hypoxic niche.

Graphical Abstract

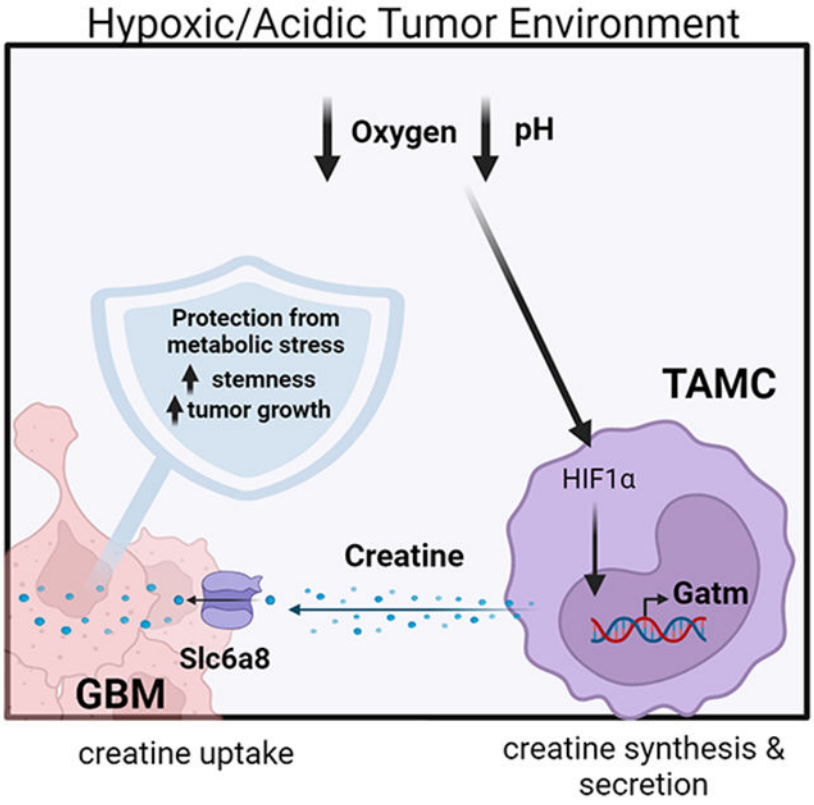

eTOC blurb

Glioblastoma (GBM), a deadly CNS malignancy, features profoundly hypoxic niches. Rashidi and Billingham et al. report that within these niches, myeloid cells upregulate creatine biosynthesis and "feed" it to tumor cells, which upregulate creatine import under metabolic stress. Therapeutic targeting of this axis provides a potential avenue for GBM treatment.

INTRODUCTION

Glioblastoma (GBM) is the most common primary CNS malignancy in adults, and even after an aggressive standard of care patients ultimately succumb to the disease [1]. The devastating impact of this disease and the lack of effective therapies create an urgent need for exploration. Numerous studies have shown that tumor-associated myeloid/monocytic cells (TAMCs) are a central factor in the growth and therapy resistance of GBM [2-7]. These TAMC populations are the most abundant cell type in GBM [8]. This myeloid-rich microenvironment appears to be specific to primary brain tumors, as brain-metastatic lesions do not mimic this myeloid-rich infiltration [9]. Therefore, primary brain tumors are unique in their proclivity to recruit TAMCs.

Despite their central role in the pathobiology of GBM, the actual role of TAMCs in promoting tumorigenicity remains elusive. Highlighting their central role in promoting GBM, perturbation of TAMCs is an efficacious method of therapy in preclinical models of the disease. Inhibiting myeloid-associated chemokine receptors [10-11], targeting TAMC depletion using PD-L1 conjugated nanoparticles [4], and pharmacological depletion of TAMCs [12] all yield significant survival benefits in preclinical models of GBM. Other strategies focus on "reprogramming" myeloid cells towards a pro-inflammatory phenotype [2-13-14] and are currently being explored in clinical trials for GBM.

To better understand the role of TAMCs in GBM we performed a comprehensive spatial, genetic, and metabolic exploration of these populations in both human and preclinical mouse models of GBM. Our analysis revealed that bone-marrow-derived TAMCs, but not microglia preferentially localized to the peri-necrotic/hypoxic niche of GBM. The peri-necrotic niche is identified by an organized cellular structure, known as pseudopalisades, which surround necrotic cores and are comprised of both neoplastic and non-neoplastic cells [15]. The relevance of these structures cannot be understated as their presence signifies poor prognosis in patients with GBM [16] and they are thought to be a central driver of disease progression [17].

Examination of the metabolic/transcriptomic phenotype of TAMCs in the peri-necrotic regions identified *de-novo* production of creatine as a hallmark metabolic signature for these cells. Interestingly, genetic expression of the creatine transporter, SLC6A8, was restricted to tumor cells characterized with hypoxic/stem cell-like signatures located directly adjacent to TAMCs. Therefore, we hypothesized that a unique role of TAMCs in GBM is to provide creatine for the hypoxic pseudopalisading niche in GBM.

RESULTS

Creatine metabolism is a hallmark of tumor-associated myeloid cells in humans with GBM.

To examine the metabolic phenotype of myeloid cells in GBM, we obtained peripheral blood mononuclear cells (PBMCs) and tumor tissue from 5 patients with newly diagnosed GBM and performed $CD163^+$ magnetic bead-based isolation (Fig. 1A-B). After isolation, we performed untargeted metabolomics and visualized the top 25 metabolite changes by p-value, plotted with Metaboanalyst (Fig. 1A). All three metabolites associated with creatine metabolism, guanidinoacetate, creatine, and phosphocreatine, were upregulated in TAMCs as compared to peripheral myeloid cells (Fig. 1B). Among the most strongly upregulated metabolites was guanidinoacetate (GAA; $p< 0.013$), which can only be synthesized by the breakdown of arginine in a process termed *de-novo* creatine biosynthesis (Fig. 1C). These data suggest that $CD163^+$ TAMCs are actively generating creatine from arginine in the GBM tumor microenvironment (TME).

To identify the spatial metabolic and genetic phenotype of creatine synthesizing cells in GBM we performed analysis of spatially resolved multi-omics and single-cell sequencing (scRNA-seq) of human GBM (Fig. 1D-K). Myeloid cells from *de-novo* GBM were extracted from the most recent pan-immune cell atlas [18] and single cells were sub-characterized by iterative SNN clustering and presented in reference-based Uniform Manifold Approximation and Projection (UMAP) as previously published (Fig 1D; [18]). The expression of *GATM* (glycine amidinotransferase) and *GAMT* (guanidinoacetate methyltransferase) was found to be significantly enriched in activated macrophages recently defined as θMa ($p_{adj}<0.00023$, Wilcoxon Rank Sum) and θMb ($p_{adj}<0.0001$, Wilcoxon Rank Sum) (Fig 1D,E). Importantly, these populations are characterized by $CD163^+$ expression, which we used as our marker for TAMC enrichment in Fig. 1A-B.

We then examined the spatially weighted correlation analysis of the integrated spatially resolved transcriptomic-metabolomic dataset [19], comparing the spatial overlap of gene expression (rows) and metabolic intensities (columns) (Fig. 1F-I). This analysis was performed for the *GATM*, *GAMT* and *SLC6A8* genes (Fig. 1F *left panel*) and myeloid cell types (Fig 1F *Right panel*). The data in *the left panel* shows that, expectedly, *GATM* expression is closely associated with both creatine, guanidinoacetate, and glycine. The *right panel* indicates that creatine is detected across most myeloid subsets with notable exception of microglia. Analysis of the spatially distinct transcriptional phenotypes associated with creatine metabolites (Fig. 1G) revealed that creatine and GAA are most closely associated with radial glia gene signatures, a phenotype associated with glioma stem cell phenotypes and migration [20]. Analysis of the Verhaak subgroups (Fig. 1H) demonstrate that the classical and mesenchymal molecular subtypes are most associated with creatine metabolites. In agreement with the scRNAseq-data, GAMT and GATM expression is most strongly spatially correlated to the myeloid cell types θMa and inversely correlated with microglial gene expression (Fig. 1I).

Critically, the spatially resolved transcriptomics displayed that θMa (defined, in part, by $CD163^+$ expression[18]), are located adjacently to the hypoxia-associated distinct regional transcriptional program, which is also the histologically defined pseudopalisading zone of

GBM tumors (Fig. 1J-K). Three specific representative examples of the spatial expression of θMa subsets, GATM expression, and the metabolites GAA and creatine can be found in Supplementary Figure 1A. This data suggest that myeloid cells with the creatine metabolic phenotype surround the hypoxic and perinecrotic regions of GBM.

To analyze in more detail which specific subpopulations express creatine biosynthetic enzymes we performed a comprehensive sub clustering of myeloid cells into 18 distinct molecular subgroups using the GBmap database (Supplementary Figure 2). This dataset contains single cell and spatial data from 26 datasets, 240 patients, and includes over 1.1 million cells (https://github.com/ccruizm/GBmap;). Examination of 1.1 million cells in GBM (Supplementary Figure 2A), identified approximately 10% of events (134,405 cells) as myeloid cells (Supplementary Figure 2B). Analysis reveals many subtypes of myeloid cells express both *de-novo* creatine genes, with the majority being expressed on bone marrow derived monocytes (BDM) and microglial populations (MG) (Supplementary Figure 2C-D). Myeloid cells exhibit different spatial localizations, such as the “BDM-hypoxia-MES” cells which are found within tumor necrosis and “BDM-anti_inf” which are located further from this niche (Supplementary Figure 2E-F). Importantly these cells express both high levels of *GATM* and *GAMT*.

Myeloid cells surround the hypoxic niche in GBM.

To validate this preferential localization of myeloid cells to the peri-necrotic niche, analysis was performed for $CD163^+$ cells by a board-certified pathologist (D.J.B) who examined the location and observed the highest $CD163^+$ expression on cells within pseudopalisades surrounding necrosis of human GBM tissue (Supplementary Figure 3A) [21]. We then used multiplex immunohistochemistry to gain a more complete picture of the TAMC and microglial location in GBM. Using carbonic anhydrase 9 (CA9) as a surrogate marker for hypoxia [22], we probed the localization of myeloid cells ($CD163^+$) in hypoxic and non-hypoxic regions of brain tumors. The data show a significant enrichment of myeloid cells in hypoxic pseudopalisading regions (P) of brain tumors as compared to non-pseudopalisading regions (NP) ($p<0.05$, Fig. 2A). Furthermore, we identified this location is only in $CD163^+$ populations, as microglial populations (defined by TMEM119 [23]) did not have the same localization (ns, Fig. 2A). Further analysis revealed a significant increase in the proximity of $CD163^+$ cells to hypoxic $Sox2^+$ cells in pseudopalisading regions of the tumor (Supplementary Figure 3B).

Examination of creatine biosynthetic proteins GATM and GAMT could also be seen surrounding the necrotic niche. Immunohistochemistry (IHC) was performed for GAMT, and GATM on five cases of primary glioblastoma, IDH-wildtype, WHO grade 4, with tissue blocks chosen for the presence of necrotic foci. We found that GAMT expression was low and variable in neoplastic cells that were distant from necrosis in GBM but was moderately expressed in cells that were immediately adjacent to necrosis, with expression diminishing with greater distance away. GATM was moderately expressed by cells that were distant from necrosis, and its expression was highest in peri-necrotic cells. The expression of creatine kinase B (CKB) is modest to moderate in neoplastic cells, with no obvious enrichment in the pseudopalisading region (Supplementary Figure 3C).

To validate that myeloid cells were indeed more likely to localize around hypoxic regions of tumors in our orthotopic GBM models, we utilized hypoxyprobe experiments to perform both immunofluorescence microscopy and flow cytometry of mice with CT-2A brain tumors.

Consistent with human GBM data, we found a propensity of $CD11b^+$ myeloid cells localized to hypoxic regions of brain tumors (Fig. 2B), and flow cytometric analysis revealed these TAMC (particularly monocytic myeloid-derived suppressor cells - MDSC) had the most hypoxyprobe signal compared to all other immune subsets analyzed (Fig. 2C). Lastly, using a Nestin-TVA driven inducible model of GBM [24], we also found a significant localization of $CD206^+$ myeloid cells in the necrotic regions but not in non-necrotic tumor tissue or normal brain parenchyma (Supplementary Figure 3D).

In agreement with the data shown in human GBM, scRNA-seq analysis of the murine CT-2A brain tumor environment revealed *Gatm* expression is robustly expressed by TAMCs (Figure 2D-F). The highest expression was in macrophages, microglia, and monocytes, with notable expression also in oligodendrocytes. Analysis of the creatine transporter (*Slc6a8*) showed that it is mainly expressed by tumor cells, and to a lesser extent oligodendrocytes (creatine uptake has been previously observed to promote oligodendrocyte function after injury [25]) and endothelial cells. These results suggest that there is an overall directionality to creatine metabolism in the hypoxic niche, wherein myeloid cells produce it and tumors uptake it.

Murine models of GBM recapitulate creatine metabolic phenotypes.

To examine and model the relevance of the *de-novo* creatine pathway in our mouse models, we examined the metabolic phenotype of TAMCs in two independent murine models of GBM (CT-2A and GL261) by implanting tumors and performing Gr1 bead-based isolation as described previously [3]. In support of our human data, we found that while levels of arginine and glycine are significantly decreased in TAMCs compared to peripheral myeloid cells ($p<0.001$ and $p<0.001$ in GL261 and CT-2A, respectively), the levels of creatine and phosphocreatine are significantly upregulated in TAMCs ($p<0.001$ and $p<0.001$ in GL261 and CT-2A, respectively) (Fig. 2G). In these initial experiments we could not detect guanidinoacetate. In support of this observation the expression of *Gatm*, the rate-limiting enzyme of *de-novo* creatine synthesis, is significantly increased in TAMCs compared to the periphery based on RNA-seq analysis (Fig. 2H). Levels of the other requisite enzymes for *de-novo* creatine synthesis, *Gamt* and *Ckb*, were found to be significantly upregulated as well in TAMCs (Fig. 2H).

To provide direct evidence of *de-novo* creatine generation, we isolated $CD8^+$ T-cells and TAMCs from the tumors of CT-2A tumor-bearing mice 14 days after tumor implantation then pulsed them for 2 hours with ^{13}C-arginine (Fig. 2I). This data revealed that M+1 creatine (natural isotopic abundance is 4%) and M+1 phosphocreatine was only detected in TAMCs but not in splenic myeloid cells or in $CD8^+$ T-cells regardless of location (9.5+/−0.04% in TAMC, not detected in other groups, $p<0.001$, ***). The data provide evidence for a cellular (myeloid) and spatial (tumor) specificity of this metabolic phenotype in GBM.

To understand the mechanisms by which TAMCs upregulate *de-novo* creatine synthesis in tumors, we reasoned that hypoxia/acidosis might contribute to this phenotype considering these cells proximity to the necrotic niche. We performed a series of assays on *in-vitro* generated tumor-associated myeloid cells [26] to look for upregulation of the rate limiting enzyme of creatine biosynthesis (*Gatm*) and *Gamt* (Fig. 3). Importantly, we found that while acidity could upregulate *Gatm* and *Gamt* mRNA expression, the combination of both hypoxia and acidity led to the most significant increase in *Gatm* and *Gamt* mRNA expression (Fig. 3A-B). The protein expression of Gatm was also significantly increased by hypoxia and acidity treatment (Fig. 3 C,E) whereas Gamt was unchanged (Fig. 3 D,F). Furthermore, to validate the western results, we perform the same assays using a quantitative western (Protein Simple platform) which also demonstrated the combination of hypoxia and acidity resulted in Gatm upregulation whereas Gamt expression was unchanged (Fig. 3G-H). This supports Gatm as the rate-limiting enzyme in creatine biosynthesis [27].

Importantly, acidity can act directly and activate hypoxia-inducible factor (HIF) signaling by sequestering von Hippel-Lindau tumor suppressor (VHL) [28], therefore Gatm upregulation by acidity and hypoxia both indicate that HIF signaling may be primarily responsible for this phenotype. To validate that indeed the HIF axis regulates this phenomenon, we used our lipid nanoparticle (LNP) platform to deliver siRNA to TAMCs which efficiently knocked-down expression of *Hif1a* or *Hif2a* (Fig. 3I). Indeed, treatment with *Hif1a* siRNA (or the combination of *Hif1a* and *Hif2a* siRNA) significantly reduced the expression of Gatm transcript and protein that was upregulated by the combination of hypoxia and acidity (Fig. 3J-K). *Hif2a* was dispensable for this upregulation.

Compartmentalization of creatine synthesis and uptake occurs in GBM

Considering our mechanistic results in murine TAMCs, we wanted to assess the location of creatine producing TAMCs in human patients with GBM relative to the histological elements known to be associated with hypoxia, acidity, and pseudopalisading necrosis [21].Referring to the spatial transcriptomics of human GBM tissues we observed expression of *SLC6A8* in the pseudopalisading region, surrounded by myeloid cells expressing of *GATM* and *GAMT* (Fig. 4A). To measure these interactions, we analyzed the spatial trajectory of the creatine transporter (*SLC6A8*) and creatine biosynthetic enzymes (*GATM/GAMT*) which highlight the non-overlapping, adjacent expression of creatine-transport and creatine-biosynthetic enzymes in different niches of human GBM (Fig. 4B). Independently supporting this observation, IVYGap database analysis reveals a specific localization of *SLC6A8* expression to the pseudopalisading/necrotic regions of the tumor cells (Supplementary Figure 4A) and its expression is significantly correlated with hallmarks of hypoxic metabolism (Supplementary Figure 4B). This is consistent with previous literature indicating that creatine transporter upregulation is a hypoxia inducible phenomenon [29-30]. Examination of previously published human scRNA-seq GBM datasets also demonstrated that expression of *SLC6A8* is significantly correlated with hypoxic and glycolytic gene signatures (Supplementary Figure 4C) and GSEA reveals that *HIF1a* signaling is positively correlated with SLC6A8 expression in these tumors (Supplementary Figure 4D)

Furthermore, CT-2A, GSC-005 and U251 glioma cell lines upregulated *Slc6a8* when placed under 1% O_2 overnight, providing additional evidence for hypoxic regulation of this transporter (Fig. 4C). More detailed analysis reveals that, unlike in myeloid cells, only hypoxia (not acidity) was responsible for upregulation of *Slc6a8* in CT-2A tumor cells, U251 human glioblastoma cell lines, and GSC-005, a genetically defined murine stem cell-like glioma cell line (4Fig. 4D). Confirming that HIF signaling controls *Slc6a8* Expression, combinatorial siRNA knockdown of *HIF1a* and *HIF2a* was able to significantly abrogate Slc6a8 in the U251 cell line (Fig. 4E-F). Therefore, the HIF axis controls both creatine synthesis and uptake in GBM.

This data suggest that TAMCs may be actively secreting creatine for tumors to take up within hypoxic regions. Indeed, the culture of *in-vitro* generated TAMCs in ^{13}C-flux media modestly decreased M+6 arginine in the media and resulted in secretion of M+1creatine into the media (Fig. 4G). When comparing splenic myeloid cells to TAMCs isolated from tumor-bearing mice, there was a significant increase in secretion of creatine and GAA into the media of TAMCs, whereas splenic myeloid cells had no observable secretion ($p<0.001$; Fig. 4H-I).

Creatine uptake supports GBM growth and survival.

To test if the uptake of creatine is relevant to the growth and survival of GBM we treated murine CT-2A cells under normoxia or 1% O_2 hypoxia for 4 hours with the inclusion of 1mM creatine and performed viability assays with Cell-Titer Glo (Fig. 5A). There was a significant increase in viability of tumor cells under hypoxia treated with 1mM creatine. We found that the survival (as measured by MTT assay) of CT-2A tumor cells under hypoxia was enhanced only under glucose-limiting conditions (Fig. 5B). To further verify the protective effect of creatine on GBM under hypoxia we performed several Cell titer Glo assays on CT-2A, GSC-005, and GL261 cell lines (Fig. 5C, *left, right, and bottom panel, respectively*). This reveals that under hypoxic and glucose limiting conditions, tumor cells have higher viability that is abrogated by the most commonly used creatine uptake inhibitor, β- guanidinopropionic acid (β-GPA) [31]. Furthermore, inhibition of creatine kinase activity using 1mM cyclocreatine [32] also blunted the pro-survival phenotypes. Therefore, the creatine phosphagen system increases glioma cell survival under stress and supports the theory that enhancement of the creatine-phosphocreatine shuttle is important for tumor growth [32]. However, other mechanisms, such as increasing import of extracellular ATP [33-34] or ameliorating oxidative stress [35] cannot be ruled out.

To examine the influence of the creatine transporter on glioma biology we generated a CRISPR-KO of *Slc6a8* in CT-2A and validated KO using quantitative PCR analysis compared to vector controls (Vc) (Fig. 5D). To validate these cells were deficient in creatine uptake we treated cells with ^{13}C-labelled creatine and measured creatine uptake after 4 hours (Fig. 5E). Analysis reveals that *Slc6a8* knockout significantly inhibited both unlabeled and labeled creatine/phosphocreatine levels within the cells. To examine the kinetics of creatine uptake, we performed a ^{13}C-creatine flux, which revealed that after 2 hours there were detectable decreases in creatine/phosphocreatine uptake by CT-2A cells (Fig. 5F). We next implanted these cells into several cohorts of mice and monitored tumor growth

(Supplementary Figure 5A-B), *in-vivo* measurement of proliferation via Ki-67 staining (Figure 5G-H) and animal survival (Figure 5I). Survival of mice implanted with Slc6a8 KO cells were significantly extended over vector control tumors, with 5/10 mice not succumbing to disease ($p<0.01$, **) (Figure 5I). In concordance with the survival curves, tumor area measurement via H&E revealed that control tumors grew faster than KO, with several KO not having identifiable tumors after 28 days (Supplementary Figure 5A-B). Examination of Ki-67 percent positivity across all tumors measured identified that Slc6a8 KO tumors have significantly less Ki-67 positivity than controls (Fig. 5G-H). This indicates that Slc6a8 promotes glioma-cell proliferation *in-vivo*.

To validate that the creatine transporter is essential in the protective effects of creatine in another cell line, we performed shRNA knockdown of Slc6a8 in U251 human glioma cell line (Fig. 5J) and performed Cell-titer glo assays as done above (Fig 5K). Importantly, we find that creatine-induced upregulation of ATP luminesce in U251 cells is abrogated by the KD cell lines (Fig. 5L), and these cells are refractory to inhibition by either β-GPA or Cyclocreatine.

Flow cytometry analysis of these tumors revealed minimal changes in immune composition in tumors, draining lymph nodes (dLN), and bone marrow of implanted mice (Supplementary Figure 7; **Gating in** supplementary Figure 6). One notable observation is the percentage of T-cells with an activated phenotype was increased in mice implanted with Slc6a8 KO cell lines. Another observation is that tumor associated macrophages (TAM: $CD45^{+}11b^{+}LY6G/C^{-}$) were found to be increased in the Slc6a8 KO tumor-bearing mice. These data suggest decrease in tumor incidence in these mice is likely related to tumor intrinsic effects of creatine transporter deficiency rather than anti-tumor immunity.

Pharmacologic inhibition of creatine uptake is a relevant therapeutic strategy for glioblastoma therapy.

To test if β-GPA could inhibit TAMC-tumor creatine transfer we designed a transwell experiment to measure metabolite transfer (Fig. 6A). To achieve this, we generated TAMCs and preloaded them with ^{13}C-arginine overnight, then the following day washed and placed them in a 3μm transwell chamber with cultured CT-2A cells on the bottom. In half of the wells, we also included 1mM β-GPA and then cultured them for 8 hours under normoxic or hypoxic conditions. As expected, tumors under hypoxia increased their uptake of ^{13}C-labeled creatine, supporting their affinity for creatine uptake under hypoxia (normalized peak area of $5.7x10^{7}\pm5.6\ x10^{6}$ in normoxia vs $8.6x10^{7}\pm4.6x10^{6}$ in hypoxia, $p<0.05$) (Fig. 6B). Importantly, we were able to reproduce these phenomena in genetically defined GSC-005 murine stem cell-like GBM lines (Supplementary Figure 8A-B). This data demonstrated a significant increase in creatine synthesized from TAMCs, and phosphocreatine (PCr) levels were significantly reduced with β-GPA treatment. We could not measure creatine and GPA simultaneously in LC-MS due to technical limitations (they are too similar in mass/charge ratio to separate). However, we could faithfully measure ^{13}C-PCr levels in these cells which demonstrated a robust decrease in PCr levels in both normoxia and hypoxia (Fig. 6B, Supplementary Figure 8B, right panel, $p<0.001$). This

indicates that the presence of β-GPA effectively blocks creatine transfer from TAMCs to tumors cells.

Our data indicates that creatine transport is most relevant to cells under hypoxic and metabolic stress. Furthermore, as we have observed that Slc6a8 expression *in-vivo* is associated with necrotic regions and stem cell rich signatures, we aimed to recapitulate these results using a tumor sphere forming assay using CT-2A vector control, or Slc6a8 KO cell lines [36] (Supplementary Fig. 8C-D;). After 14 days of culture in stem cell media, sphere size in CT-2A tumor cells was measured via microscopy (Supplementary Figure 8C-D) and cell survival was measured via flow cytometry (Supplementary Figure 8E). In vector control cells, the addition of creatine led to an enhanced sphere size, an effect abrogated by β-GPA treatment. The combination of Cr + β-GPA led to both significantly reduced sphere size and increased apoptosis. Highlighting the necessity of Slc6a8 in these observations, Slc6a8 KO cells were unaffected by Cr or β-GPA treatment. Thus, creatine can promote *in-vitro* tumor sphere growth, while β-GPA can prevent the growth and viability of these cells in stem cell cultures.

To examine more directly the role of creatine in stem cell biology we performed extreme limiting dilution assays (ELDA) on the tumor line GSC-005, a genetically defined glioma line known for its stem cell like properties [37] (Fig. 6C). This data revealed that creatine treatment significantly enhances stemness under hypoxic treatment, and this was abrogated with β-GPA treatment. ELDA assays were also performed in human PDX line GBM 39, with data showing that β-GPA treatment could significantly prevent stemness (Supplementary Figure 9). Therefore, creatine may promote stem cell phenotypes in GBM, and this is prevented using an inhibitor of creatine transport.

To examine if blockade of creatine uptake is effective *in-vivo*, we gave mice a β-GPA disodium salt currently in phase I clinical trials, RGX-202-01 [33-38]. Supplementation via chow started 7 days, post tumor implantation, in three orthotopic preclinical murine models of GBM. (Fig. 6D-F). While monotherapy with RGX-202-01 only promoted animal survival in GL261 tumors (median survival 17.5 Days in Control and 24.5 days in RGX-treated; $p<0.001$ ***), radiation worked in concert with RGX-202-01 to significantly promote animal survival in CT-2A, GL261, and GSC-005 tumor models. Therefore, pharmacologic blockade of creatine transfer between TAMCs and tumors may be a therapeutically relevant treatment for GBM.

Flow cytometry analyses of these treatment modalities reveal some changes to immune composition of CT-2A and GL261 tumor-bearing mice following treatment (Supplementary Figures 10 and 11, respectively). Within CT-2A tumors, there was a significant reduction in regulatory T cells with radiation, which was exacerbated by RGX-202-01 treatment. In GL261, the combination also showed this reduction (albeit not significantly). In the dLN of CT-2A Tumor bearing mice, radiation treatment increased $CD8^+$ T-cell activation, indicating increased anti-tumor immunity is being observed. Interestingly, in GL261 mice, the combination of RGX-202-01 and radiation resulted in an additive effect to CD8 T-cell activation within the dLN.

The myeloid compartment in CT-2A tumors was also perturbed by radiation and RGX treatment. RT resulted in an increase in Monocytic-MDSC like cells expressing MHC-II, whereas combination therapy resulted in an increase in the ratio of these Monocytic-MDSC cells compared to other myeloid subsets. Surprisingly, the effects of RT on the myeloid composition in GL261 was not consistent with the CT-2A model. For example, the combination of RGX-202-01 and RT reduced MHC-II expression by Monocytic MDSCs in the GL261 model. RT dramatically increased Myeloid/T-cell ratios in GL261 tumors, which was abrogated by RGX-202-01 administration. Therefore, the combination of Radiation and RGX-202-01 therapy exerts several changes in the immune landscape of these tumors.

Lastly, to demonstrate that myeloid-derived creatine can influence animal survival we generated murine conditional knockout of GATM in myeloid cells using the Cre-lox system. To achieve this, we crossed LysM-Cre mice with *Gatm*-floxed mice [39], and validated that reduction of *Gatm* expression, using western blot (Fig. 6G; *top panel*) and qPCR analysis (Fig. 6G; *bottom panel*) on *in-vitro* generated TAMCs. We also validated that myeloid cells were deficient in creatine production by monitoring M+1 creatine flux over time *in-vitro* (Fig. 6H *left panels*). Conditional knockout of *Gatm* had no effect on the production of ornithine and putrescine which are known to be used by TAMCs to survive within the acidic and hypoxic tumor regions [3] (Fig. 6H *right panels*). Supporting the role of myeloid-derived creatine's influence on tumor growth, we implanted littermate control and Gatm-cKO mice with CT-2A tumor cells and monitored survival. This revealed a significant increase in survival of Gatm-cKO mice (Median survival Control 23 days vs 29 days for cKO; $p<0.01$) (Fig 6I). Flow cytometry analysis of the TME of the mice reveal minimal changes to the TME with no observable difference in myeloid phenotypes (Supplementary Figure 12). This suggests that creatine synthesis by myeloid cells is mainly influencing tumors. Therefore, the *de-novo* synthesis of creatine enhances preclinical murine model GBM growth *in vivo*.

DISCUSSION

The results of this study indicate a role for myeloid cells to act as "feeder-cells" and to provide creatine for tumors to enhance their growth both *in-vitro* and *in-vivo.* As *de-novo* creatine synthesis typically occurs in the kidney by proximal tubule cells, it is surprising that myeloid cells acquire this phenotype in GBM. However, each TME is complex and unique, and we have also demonstrated that extracellular acidity and hypoxic signaling via *Hif1a* is responsible for creatine biosynthetic phenotypes. The fact that this pathway also feeds into ornithine generation reveals two important details. Firstly, GATM activity may increase polyamine generation of myeloid cells, and the acquisition of a polyamine metabolic phenotype is already known to associate with immunosuppression [3], and tissue repair [40-41] in GBM. Secondly, this pathway may be a cellular mechanism utilized to subvert arginase-1 inhibition, which is currently in the clinic for immune suppression [42].

It is unclear why tumor cells in hypoxic and necrotic regions have a dependence on creatine intake, but there are potential explanations that may provide insight. One explanation comes from a recent report that showed creatine promoted synergistic effects with hypoxia through upregulation of the glycine cleavage system and chemical regulation of prolyl-hydroxylase domain resulting in a reduction of reactive oxygen species for GBM cells in hypoxic

conditions [43]. This in turn protected GBM cells against hypoxia-driven cell death which highlights the essential role of creatine synthesis within hypoxic regions.

A second explanation is that creatine transport is incredibly important regarding CNS health, as evidenced by the germline mutations in Slc6a8 leading to severe mental retardation [44]. There is also extensive literature regarding the neuroprotective effects of creatine [45-47]. Therefore, brain tumors may be predisposed to taking up creatine due to their location relative to other tumors and the unique role of the blood-brain barrier. A second possibility lies in the metabolic choices of tumors regarding arginine metabolism.

A third option comes with the metabolic cost of producing creatine. Creatine synthesis is a costly process and requires the input of arginine, glycine, and methionine (in the form of S-adenosyl methionine – SAM). Specifically, creatine biosynthetic processes use 20-30% of arginine's amidino groups, and 40% of the active methyl groups in a cell [48]. This is an enormous burden to a cell, especially if a cell needs to undergo the broad epigenetic changes associated with a migratory/stem cell state in the hypoxic niche. Indeed, we found that creatine promotes stemness in GBM cells, which was abrogated by inhibiting creatine transport. Furthermore, supporting the need of additional creatine in GBM, extensive studies on MR-spectroscopy demonstrate that creatine levels are lower in GBM tissue compared to normal brain tissue [49-52], and reduced in GBMs with higher degrees of necrosis [50-51]. Thus, creatine levels are generally reduced in GBM, and one functional aspect of TAMC recruitment by these tumors is to provide creatine to promote survival under hypoxic stress.

It is unclear why tumor cells in hypoxic and necrotic regions have a dependence on creatine intake, and why this results in a reduction in tumor engraftment, but there are potential explanations that may provide insight. In brain tumors, there are widespread regions of necrosis and hypoxia throughout the tumor not just a single necrotic core as commonly envisaged [53-55]. Therefore, ablation of creatine transport may play a larger role in halting tumorigenesis than one might expect. Future studies are aimed at using inducible models of GBM to determine the exact role of creatine transport in the initiation of brain tumors.

It is clear based on our study that a compartmentalization of creatine synthesis and uptake occurs in GBM between myeloid cells and tumor cells. This compartmentalization may occur in other solid tumors categorized with enriched hypoxic regions and myeloid infiltration. This study focuses on the exchange of metabolites within a specific niche in GBM but does not address the role of creatine metabolism in other tumor regions. There are other populations, such as microglia (which are not enriched in hypoxic/pseudopalisaing niche), which can also express creatine biosynthetic enzymes. Future studies will aim to understand the role of creatine in other tumor niches in GBM. Another unanswered question is, does perturbation of creatine transport prevent formation/stability of the pseudopalisading hypoxic niche? As presence of this niche negatively portends patient outcomes [15-16-17,] it is possible that targeting this axis may yield clinical improvement in patients with brain tumors. Future work will be aimed at understanding this possibility.

While the effects of creatine uptake inhibition are limited as monotherapy, combination with other anticancer agents have shown significant promise in other tumors [33-34-38] – and our

work highlights a potential but variable combinatorial effect with radiation that warrants further investigation. An important issue surrounding the targeting of creatine metabolism as a therapeutic is creatine metabolism is essential for productive T-cell responses. Di Biase et al. demonstrated that creatine enhances $CD8^+$ T-cell anti-tumor responses, which could also potentiate anti-PD1 responsiveness to subcutaneous models of melanoma [56]. In another recent study it was found that creatine transport and kinase activity is required for $CD8^+$ T-cell immunity [57].

The same may also be true for myeloid cells. Several studies have identified a critical role of creatine in myeloid cell/macrophage function. In one impactful study authors found that creatine uptake is essential for M2-like responses involving a mechanism of suppressing M1-like signaling and enhancing chromatin remodeling [35]. Conversely, another recent study highlighted that covalent inhibition of creatine kinase inhibited M1-like inflammatory responses by macrophages [58]. In a recent study by our group, we found that creatine kinase activity is critical for promoting NLRP3 inflammasome activation in macrophages [59]. Its role within myeloid cells of brain tumors is still to be determined, but considering previous studies, it likely exerts an important role. Therefore, therapeutically targeting creatine metabolism may have unintended consequences on host immunity that must be considered when running trials on these compounds.

LIMITATIONS OF STUDY

There are several limitations and associated future directions related to this work. Firstly, we assayed the effects of creatine perturbation on stem cell phenotypes using ELDA assays, which is only one assay to test stemness in tumor cells. Furthermore, the mechanisms by which creatine promotes stem cell phenotypes is not described. Future studies are aimed at dissecting the mechanisms by which creatine influences stemness in tumors.

One limitation to consider is that RGX-202-01 represents a pioneering effort as the sole compound in clinical development aimed at modulating creatine metabolism. This unique compound, designed to mimic creatine metabolism, presents specific challenges when used in brain tumor treatment. To maintain the desired therapeutic effect, consistent high concentrations are required, which can be demanding given the tight regulation of guanidino compounds at the Blood-Brain Barrier (BBB) [60]. Consequently, future research endeavors are directed towards exploring more potent and highly specific inhibitors of creatine metabolism, including recently developed covalent inhibitors of creatine kinases [58].

STAR METHODS

RESOURCE AVAILABILITY

Lead contact—Further information and requests for resources and reagents should be directed to and will be fulfilled by the Lead Contact, Jason Miska (Jason.miska@northwestern.edu).

Materials availability—This study did not generate new unique reagents.

Data and code availability

- RNA-seq data have been deposited at GSA and are publicly available as of the date of publication. The accession number of the Bioproject is listed in the key resources table.
- Metabolomics data sets have been deposited in Metabolomics Workbench and are publically available. The study number of the project is listed in the key resources table.
- All software used is provided in the previous publications [18-19]. All raw data used to generate the figures throughout the manuscript can be found within the Data S1 document.
- This paper does not report original code.
- All additional datasets included in the manuscript will be provided upon request from the Lead Contact.

EXPERIMENTAL MODEL AND STUDY PARTICIPANT DETAILS

Mice—All mice were housed at the Center for Comparative Medicine at Northwestern Feinberg School of Medicine. Mice were all housed in a conventional barrier facility with 14-hour light/10-hour dark cycles and ad libitum access to food and water. C57/Bl and LysM-Cre mice (C57/Bl6 background) were obtained from The Jackson Laboratory (Bar Harbor, ME) and bred for use in experiments. Animals were raised and accommodated in a conventional barrier animal facility at Northwestern University, adhering to a 14:10 light:dark cycle, maintaining an ambient temperature of 22 °C, and a relative humidity range between 30-70%. Both experimental and control animals were housed together. GATM-flox mice were obtained from the Spiegelman laboratory [39]. Nestin-^{TVA} P53$^{fl/fl}$ PTEN$^{fl/fl}$ mice were housed in the laboratory of D.J.B. Experiments were performed in mice 6 to 8 weeks old, age- and sex-matched. Equal numbers of male and female mice were used for all survival curves except for the Gatm cKO experiment. All mice used were on the C57/Bl6 genetic background. Littermate controls were employed in all experiments, except for those involving the *ad-libitum* water administration of RGX-202-01. Health checks for mice are performed daily by both CCM and staff and laboratory personnel. For all Kaplan-Meier curves involving C57/Bl6 mice, they were purchased at 6 weeks old, and numbers of male/female mice were always equivalent between control and experimental groups. For all experiments involving animal survival, no differences between sexes were observed in any experiment, so the data is not shown. All mouse protocols performed in this study were approved by Northwestern's Institutional Animal Care and Use Committee under study approval number IS00017401.

RCAS-tv/a model—5x10^5 DF-1 cells (chicken fibroblasts) expressing RCAS-PDGFB or RCAS-Cre (1:1 ratio) were stereotactically injected in nestin-tv/a (RCAS receptor) TP53$^{flox/flox}$ PTEN$^{flox/flox}$ mice generating Proneural subtype GBMs. Tumors were allowed to grow for 3 weeks, and animals were examined by Magnetic Resonance Imaging (MRI) to verify tumor growth before euthanasia. MRI images were captured using a Bruker 7T ClinScan MRI system operated via a Siemens Syngo platform. Anesthesia was maintained

throughout the scan session. Specific details regarding acquisition parameters is described previously [61].

Cell Culture

Glioma cell lines and tumor implantation: The CT-2A tumor line was initially obtained from Sigma/Millipore. The GL261 tumor line was purchased from the National Cancer Institute (NCI). Cells were cultured in Dulbecco's modified Eagle's medium (Corning) supplemented with 10% fetal bovine serum (FBS; HyClone) and penicillin-streptomycin. All cells were cultured at 37°C and at 5% CO_2 and 21% O_2 For normoxia experiment, 1 %O_2 was used for all hypoxia experiments. GSC-005 cells were obtained as a gift from Prof. Samuel Rabkin. GSC-005 were cultured in ReNcell NSC media (Millipore) supplemented with N2 (Invitrogen, Carlsbad, CA, USA), B27 (no Vitamin A; Invitrogen), 20 ng/mL FGF-2 (R&D) and 20 ng/mL EGF (R&D). For injections, cells were lifted with trypsin-EDTA (Corning), washed with phosphate-buffered saline (PBS), and suspended at a concentration of 1×10^5 cell per 2.5 µl for CT-2A tumors, $1x10^5$ for GL261 tumors and $1x10^4$ for GSC-005 tumors. Mice were implanted with tumor using a stereotactic apparatus following the exact specifications as described previously [62]. For experiments involving RGX-202-01 treatment, Purina 5001 chow (Catalogue 5001*) was supplemented with 500mg/kg of RGX-202-01 provided by Inspirna and was available ad libitium to mice. For whole-brain irradiation, mice were anesthetized, had their bodies shielded by 2cm thick lead plates, and given 3gy gamma-ray photons (cesium-137 source) per day for 3 days (a total of 9gy).

Neurosphere assays: Extreme Limiting Dilution Analysis (ELDA) was applied to this study. Human GBM cell lines (GBM6, GBM39 and GBM43 cells) and murine Glioblastoma stem cell line (GSC-005) were cultured as described. They were then trypsinized, washed with PBS, and plated in serial dilutions, specifically 200, 150, 100, 50, 25, 12, 6 and 3 cells per well. Each dilution was performed in 12 replicates. Cells were maintained in neurobasal media (Gibco) supplemented with N2 (Invitrogen, Carlsbad, CA, USA), B27 (no Vitamin A; Invitrogen), and basic fibroblast growth factor (bFGF; 10 ng/mL; Invitrogen), epidermal growth factor (EGF; 10 ng/mL; Invitrogen). Cells were treated either with 1mM Creatine in the presence or absence of equimolar SLC6A8 inhibitor, 3-Guanidinopropionic acid (Sigma, Cat. No. G 6878). After 7 – 10 days, neurospheres with a diameter greater than 200 um were counted. Counts were analyzed using the Walter + Eliza Hall Institute of Medical Research platform (http://bioinf.wehi.edu.au/software/elda/). This platform allows for the determination of stem cell frequency and quantification of significant differences between groups.

Patient samples

Untargeted Metabolomics: All 5 samples used for untargeted metabolomics were from patients with newly diagnosed IDH^{wt} Grade 4 glioblastoma. Tissues and PBMCs were processed immediately following isolation. All samples obtained were covered under IRB #STU00095863-MOD0032 which was approved by the Northwestern Institutional Review Board (IRB). Consent for the study was obtained by a clinical team member (physician or advanced practice nurse). The consent form was discussed with the patient,

and any questions were addressed immediately. Surgical patients provided consent during preoperative care, while patients not scheduled for surgery did so in the neuro-oncology clinic. If cognitive ability was diminished, standard hospital procedures for a healthcare agent were followed. Patients returning for related neurosurgical procedures did not require re-consent unless for new biospecimen collections. Patients were informed that they could withdraw their consent at any time. The age, sex and race of all patients used can be found in the Data S1 supplement, under the Figure 1 tab.

Spatial Trancriptomics/metabolomics: All Spatial datasets are derived from patients with GBM as described in [18-19]. Briefly The University of Freiburg's local ethics committee approved the data evaluation, imaging procedures, and experimental design under protocols 100020/09 and 472/15_160880. The methods adhered to the approved guidelines, and written informed consent was obtained from all subjects. Spatially resolved transcriptomics (stRNA-seq) were conducted on twenty-eight specimens (patients n=20), yielding 88,793 individual transcriptomes across various age groups and anatomic regions. Additionally, spatially resolved metabolomics (matrix-assisted laser desorption/ionization [MALDI]) was performed on six specimens from six patients.

METHOD DETAILS

Generation of single gene knockout of Slc6a8—Single gene knockout clones were generated in lentiCRISPRv2 (one vector system). The vector backbone was purchased from Addgene (lentiCRISPR v2 was a gift from Feng Zhang (Addgene plasmid # 52961 ; http://n2t.net/addgene:52961 ; RRID:Addgene_52961) [63]. The protocol for guide cloning and generation of the virus was as described in [63]. The guide sequence for mouse SLC6A8 KO is "CACCGGTGACCAGCTTGCTGACCGC" and non-targeting control (NTC) is "CACCAATATTTGGCTCGGCTGCGC". The SLC6A8 beta KO and control clones were selected using puromycin from Sigma (2ug/ml) in CT-2A mouse glioma cell lines.

For the U251 cell-line, knockdown of SLC6A8 was performed using lentiviral particles containing shRNA against human SLC6A8 purchased from Genecopoeia (Genecopoeia, Rockville, MD). Cells were spin-infected with particles for 2 hours at 37 °C at 850 RCF, after which these cells were plated and maintained in culture undergoing selection using puromycin treatment from Sigma (2ug/ml). Knockdown efficiency was determined via western blot and qPCR analysis.

The SLC6A8 KO and KD (CT-2A and U251, respectively) was confirmed using western blotting (SLC6A8, Proteintech; 1:1000 dilution, 20299-1-AP).

MTT Cell Viability Assays—MTT viability assays were conducted using the chemical 3-[4,5-dimethylthiazole-2-yl]-2,5-diphenyltetrazolium bromide (MTT). Briefly, cells were plated at a density of $1x10^4$ per well in a 96-well plate with 6-8 replicates per condition. Following the appropriate time with conditioned treatments, the media was aspirated, and cells were treated with MTT solution following the manufacturer’s protocol (Invitrogen). The plate was read out at an absorbance of 570nm.

CT-2A Sphere cultures—Adherent monolayer CT-2A cells plated into DMEM/F-12 medium containing 20 ng/ml epidermal growth factor (R&D Systems Inc, Minneapolis, MN), 20 ng/ml basic fibroblast growth factor (R&D Systems, Inc, Minneapolis, MN), B27 supplement 50x (Invitrogen, Carlsbad, CA). Cells were incubated at 37°C in humidified air with 5% CO_2. Supplemental treatment conditions were added every 48 hours. After spheres were initially formed under these culture conditions, they were dissociated with accutase and expanded for several passages before assays were performed. At 14 days, neurosphere images were collected. Following imaging neurospheres were centrifuged at 1200rpm for 5 minutes. Cells were resuspended and enzymatically dissociated with accutase (A111050, Thermo Scientific),, washed once with ice-cold PBS, and stained for live/dead using APC-Efluor780 viability dye measured with flow cytometry.

Quantitative PCR—RNA extraction was performed using Qiagen RNEasy kits (Qiagen, Hilden, Germany) or using the Omega E.Z.N.A. RNA Isolation Kit (R6834-02, Omega Biol-tek, Norcross, GA) per manufacturers protocols. The cDNA was generated from RNA samples with an iScript kit (BioRad, Hercules, CA, USA) per manufacturer's protocol. Reactions were set up using standard amounts of cDNA, SybrGreen (Biorad), forward and reverse primers (IDT, Newark, NJ, USA) and read out on CFX96 qPCR machine (Biorad). All primers were generated from Primer-BLAST using the fixed settings. Reactions were performed in triplicates. The following primers were used: SLC6A8 (human) (forward 5' GACACGCCAGATGGACTTCA-3'; reverse 5'-GATTCCTCCAACCAGGGCAA-3') Slc6a8 (mouse) (forward 5'-GACACGCCAGATGGACTTCA-3'; reverse 5' GATTCCTCCAACCAGGGCAA-3'), Gatm (mouse) (forward 5'-GCTTCCTCCCGAAATTCCTGT-3'; reverse 5'-CCTCTAAAGGGTCCCATTCGT-3'), b-Actin (mouse) (forward 5′-CTAAGGCCAACCGTGAAAA-3′; reverse 3′-ACCAGAGGCATACAGGGACA-5′). b-Actin (mouse) (forward 5′-CCTGGCACCCAGCACAAT-3′; reverse 3′-GCTGATCCACATCTGCTGGAA-5′). Fold changes in gene expression relative to untreated control were calculated by the ΔΔCt method using mouse actin as an endogenous control for mRNA expression.

Wes (ProteinSimple) Protein Quantification

Protein concentration was determined via Bradford Assay. Immunoblot was performed on the Wes (ProteinSimple) using equal amounts of protein per sample according to the manufacturer's instructions for GATM (#2118, Cell Signaling Technology, Danvers, MA), GAMT (12801-1-AP, Proteintech, Rosemont, IL), or GAPDH (10880-1-AP, Proteintech, Rosemont, IL). Chemiluminescence of all proteins was quantified on Compass software (v.5.0.1; ProteinSimple). Relative protein expression levels were quantified as peak area of GATM or GAMT over GAPDH.

Cell-Titer Glo viability and intracellular ATP Assays—Cells were seeded in a 96-well flat bottom white plate at a density of $1x10^4$ cells/well in 100ul complete DMEM. Twelve hours after seeding, cells were checked for adherence and the media was aspirated and replaced with conditioned treatment media. Following treatment, the Cell-Titer Glo assay was done following manufacture's protocols (Promega, Madison, WI, USA). The

plate was placed in a BioTek Cytation5 plate reader and luminescence signal was measured with the following settings: Luminescence, Read Type: Endpoint/Kinetic, Optics Type: Luminescence Fiber, Gain: 135, Integration Time: 0:01.00 (MM:SS.ss), Read Height: 1.00mm.

Tissue isolations/analyses

Magnetic bead isolation of cells: To isolate specific populations of cells, single-cell suspensions as isolated above were preblocked with anti-CD16/32 for 15 min at 4°C. We then used the biotinylated anti-Gr1 (clone RB6-8C5), anti-CD8β, or anti-CD163 antibodies (all from Thermo Fisher Scientific) to label murine myeloid, $CD8^+$, and human monocytes, respectively. Next, the cells were washed and then incubated with anti-biotin magnetic beads (Miltenyi Biotec) before performing manual positive selection using MS columns (Miltenyi Biotec). Purified cells were analyzed for all downstream metabolic analyses.

In vitro tumor-association macrophage generation: Bone marrow precursors were isolated from the femurs of C57/Bl6 mice and resuspended in RPMI supplemented with recombinant macrophage colony-stimulating factor (M-CSF) (40 ng/ml). After 3 days, cells were washed and replaced with the same medium + 50% of 0.2-μm sterile-filtered CT-2A supernatant

Lipid nanoparticles siRNA encapsulation: were synthesized using an ethanol injection method. Briefly, D-Lin-MC3-DMA (BroadPharm), cholesterol (Sigma), 1,2-distearoyl-sn-glycero-3-phosphocholine (DSPC), and 1,2-dimyristoylrac-glycero-3-methoxypolyethylene glycol-2000 (DMG-PEG2000) were mixed in ethanol at a molar ratio of 50:36.5:10:2.5. The lipid solution was rapidly mixed with siRNA (Sigma) dissolved in citrate buffer (pH 4) at a ratio of 1:3 (v/v), following by dialysis against DPBS using a Pur-A-Lyzer dialysis kit (MWCO 6-8 kDa, Sigma) overnight at 4°C. The cells were treated with LNP/siRNA at a siRNA concentration of 100 nM.

GATM/GAMT upregulation studies: For upregulation of GATM/GAMT, BMDMs were washed with PBS and media was exchanged for RPMI containing 10% FBS and 1% penicillin/streptomycin and 1mM glucose. Cells were then cultured at 20% oxygen (normoxia) or 1% oxygen (hypoxia) with or without DMOG (100uM; Sigma, Cat No D3695), PT-2385 (10uM; MedChemExpress, Cat No HY-12867). Acidic RMPI was prepared to a pH of 6.7 using HCl. Samples were treated for 6h (RNA) or 24h (protein).

SLC6A8 upregulation studies: For upregulation of SLC6A8, CT-2A, GSC-005, and U251 cells were washed with PBS and media was exchanged for neutral or acidic DMEM containing 10% FBS and 1% penicillin/streptomycin. Cells were then cultured at 20% oxygen (normoxia) or 1% oxygen (hypoxia) for 24h.

Histology and immunofluorescence

Hypoxyprobe experiments: For all experiments involving hypoxyprobe, tumor-bearing animals were injected intravenously with 60mg/kg pimonidazole 30-60 minutes before harvesting tissues. For immunofluorescence: tumors were flash frozen in OCT (Fisher

Scientific) and sectioned into 7-8μm slices using a CM1860 cryostat (Leica, Wetzlar, Germany). Sections were fixed in pre-chilled acetone then stained overnight at 4°C with 1:100 anti-pimonidazole FITC (Hypoxyprobe inc.)) and CD11b-Alexa Fluor 647 1:100 (Biolegend) in antibody staining buffer - 0.5% Triton X-100 and 1% BSA (Sigma) in PBS (Boston Bioproducts, Ashland, MA). The following day samples were mounted using Fluoroshield with DAPI (Sigma). Images were taken with a Leica DMi8 microscope with a 20X objective and quantified using ImageJ. For flow cytometry: tumors were harvested into single cell suspension and blocked with anti-CD16/32 for 10 minutes before staining for surface markers: Live/Dead eFluor 780 (Thermo Fisher Scientific), anti-CD45 BV510, anti-CD3 PE-Cy7, anti-C11b BV711, anti-Ly6C Alexa-Fluor 700, anti-Ly6G Percp–cy5.5, anti-CD4 BUV395, and anti-CD8–BV605. For Intracellular/hypoxyprobe staining, anti-Foxp3 eFluor 450 and anti-pimonidazole FITC was stained following the fixation/permeabilization (Invitrogen, Thermo Fisher Scientific) protocol for intracellular flow cytometric analysis. All colors were compensated with single color controls from splenic tissues. Analysis was performed using Flow-Jo software (Becton Dickinson). All antibodies are purchased from BioLegend except Foxp3-Efluor 450 (Thermo Fisher Scientific) and anti-pimonidazole (Hypoxyprobe inc).

Immunohistochemistry – CD206: Formalin-fixed paraffin embedded mouse tumor sections were prepared using standard methodology. Samples were stained with primary antibodies for Iba1 (IBA1-0020, Aves, macrophages) and CD206 (MCA2235, BioRad, M2-like macrophages) then counterstained with DAPI (nuclei). Macrophage markers were visualized using anti-chicken (A-32931, Invitrogen) and anti-rat (A-21434, Invitrogen) fluorescent secondary antibodies. Sections were imaged using an Axio Imager.Z2 with a Plan-Apochromat 10x/0.45 M27 objective and Axiocam 503 camera (Zeiss). Fluorescence was analyzed using ImageJ (NIH) software. First raw images were filtered using a Gaussian Blur with a 5.00 sigma. Channels thresholds were set using Li for IBA1 and IsoData for CD206. Particles were quantitated within the bounds of 30-inf pixel units. Data displays dual positive areas (CD206 positivity within $IBA1^+$ macrophages) from indicated tumor regions. Adjacent normal images were captured in the contralateral hemispheres of tumor bearing mice. N = 4 regions per mouse, n = 2 mice per condition.

Immunohistochemistry – GATM/GAMT/Ki-67: Standard immunohistochemistry analysis was performed on patient specimens containing representative sections of pseudopalisades with GAMT (Novus NBP2-14036) diluted at 1:100 and GATM (Proteintech 12801-1-AP) diluted at 1:1000. For Ki-67 staining, standard immunohistochemistry analysis was performed on mouse brain samples with Ki67 (Abcam ab16667) diluted at 1:500. Four-micrometer thick sections of FFPE tissue on charged slides were warmed in the oven at 60°C for 60 minutes before deparaffinization and re-hydration. Antigen retrieval was achieved using a pH6 retrieval buffer (Biocare Reveal) in a decloaker reaching 110°C for ten minutes. Slides were cooled to room temperature and washed in TBS before neutralizing endogenous peroxidase (Biocare Peroxidase 1). Slides were then treated with a serum-free casein background block (Biocare Background Sniper) before incubation in a 10% goat serum block for 60 minutes at room temperature. Primary antibody was then added to the slides for overnight incubation at 4°C. After incubation, slides were washed well with

TBS-T before incubating in HRP polymer (Biocare MACH 2 Rabbit HRP Polymer). Finally, reaction products were visualized with DAB (Biocare Betazoid DAB Chromogen Kit). Slides were then counterstained with hematoxylin, dehydrated and mounted with xylene-based mounting media

Quantitative pathology measurements: For tumor area measurements using H&E slides, QuPath software was used, and magic wand tool was used to select tumor area, which was verified by manual confirmation. Tumor area is then automatically calculated as μm^3. For Ki-67 positivity, the entire tumor in each sample was labeled with magic wand, and 'positive cell selection mode' was used with the following changes from predefined parameters: detection image - optical density sum, intensity parameters – threshold of 0.05, intensity threshold parameters 0.1. % positivity is then automatically calculated.

Multiplex immunofluorescence staining: Sections of 5-μm thickness were obtained from formalin fixed paraffin embedded GBM. Deparaffinization of the slides was achieved using BOND Dewax solution followed by heat-induced epitope retrieval using BOND epitope retrieval solution (pH6) or pH9 EDTA buffer for 20 minutes. Slides were then subjected to peroxide and protein block. Primary antibodies were diluted with 1x Opal Antibody diluent/block solution and were coupled with the indicated Opal dyes: 1) TMEM119 (cat HPA051870, Sigma-Aldrich, 1:250 dilution) with Opal 520 (1:100 dilution), 2) SOX2 (cat ab92494, clone EPR3131, Abcam, 1:5000 dilution) with Opal 620 (1:150 dilution), 3) CA9 (cat NBP1-51691, 2D3, Novus Biological, 1:500) with Opal 540 (1:200 dilution), 4) CD163 (cat ab213612, clone EPR19518, Abcam, 1:600 dilution) with Opal 570 (1:800 dilution). Multiplex staining was performed in multiple cycles involving a heat-induced epitope retrieval step, protein blocking, epitope labeling, and signal amplification. Once all markers were stained, spectral DAPI was used to counterstain the slides and were mounted using Prolong Diamond Antifade mount.

Microscopy and analysis of multispectral images: Multispectral images (MSI) were performed using the Vectra 3 Automated Quantitative Pathology Imaging System from Akoya Biosciences. Initially, whole slide images were acquired after auto adjusting focus and signal intensity. Then, MSI was acquired in the tumor regions delineated by a certified neuropathologist (D.J.B) at 20x of original magnification. For analysis of MSI, a spectral library was created for all Opal dyes to subject acquired data to spectral unmixing that enabled the identification and separation of weakly expressing and overlapping signals from background to visualize the signal of each marker in inForm Tissue Finder software (inForm 2.6, Akoya Biosciences). Within inForm, the adaptive cell segmentation feature was used to identify nucleus of the analyzed cells and to determine the nuclear and cytoplasmic compartments on each cell. After performing the identification of each marker ($SOX2^+$, $TMEM119^+$, $CD163^+$, and $CA9^+$) using a training algorithm within inForm, all cells were automatically assigned to a specific phenotype. Exported files from inForm were processed in R using R packages Phenoptr and PhenoptrReports to merge and create consolidated single files for each tumor sample. Consolidated files contained single and double phenotypes as outputs that we employed for further quantification and spatial analyses using the Phenoptr R add-in.

Quantification of cell types and spatial analysis of GBM samples: Merged and consolidated files were analyzed using Phenoptr to quantify the cell density of $SOX2^+$ $CA9^+$, $CD163^+$, $TMEM119^+$. For the spatial analysis, mean cell counts within a specified radius of 15 μm from a given cell type to another cell type were calculated using Phenoptr as an R add-in. Then, mean distances between the nearest neighbors were calculated from cell type of interest to other cell types. The spatial map viewer add-in within R allowed the visualization of nearest cell neighbor between selected phenotypes in a single field. Cartoons were created using Adobe Illustrator version 22.1.0.

Metabolomics Analysis

Arginine flux: SILAC RPMI medium (Fisher) was supplemented with 10% dialyzed FBS (Fisher), glycine (40 mg/ml), and U^{13}C-arginine (200 mg/ml; Cambridge Isotope Laboratories). All TAMCs were washed with blank SILAC before being reconstituted in ^{13}C medium at a concentration of 1×10^6 to 2×10^6 cells/ml for times outlined in the text. Cells, either TAMCs or tumor cells were lifted and washed twice with PBS before pellets were flash-frozen and stored at −80°C until metabolite extraction. Pellets were resuspended in 80% methanol/20% H_2O and then lysed by 3× cycles of heat shock (LN2 freezing followed by 42°C water bath). Samples were then spun at 14,000 rpm for 15 min; supernatant was collected and analyzed as described below.

^{13}C-creatine uptake: Phenol free DMEM (Fisher) medium was supplemented with 10% dialyzed FBS (Fisher), and 1mM ^{13}C-creatine (guanidino-13C, 99%). At different time point, tumor cells were lifted and washed twice with 0.9% saline before pellets were flash-frozen and stored at −80°C until metabolite extraction. Pellets were resuspended in 80% methanol/20% H2O and then lysed by 3× cycles of heat shock (LN2 freezing followed by 42°C water bath). Samples were then spun at 14,000 rpm for 15 min; supernatant was collected and analyzed as described below.

Method for Sample Reconstitution after Extraction: Extraction solution was dried using SpeedVac. 60% acetonitrile was added to the tube for reconstitution following by overtaxing for 30 sec. Samples solution was then centrifuged for 30 min @ 20,000g, 4 °C. Samples were analyzed by High-Performance Liquid Chromatography and High-Resolution Mass Spectrometry and Tandem Mass Spectrometry (HPLC-MS/MS) exactly as previously performed [3].

scRNA-seq Assays: To prepare cells for scRNA-seq, CT-2A tumors were microdissected after 14 days of tumor growth and dissociated into single cell suspension using the adult brain dissociation kit (Miltenyi) per manufacturer protocol. To enrich for immune cells, $CD45^+$ cells were then isolated via magnetic bead-based isolation (Miltenyi). $CD45^+$ and $CD45^-$ cells were then mixed at a ratio of 10:1to obtain transcriptional signatures of both immune cells ($cd45^+$) and tumor cell ($CD45^-$). Samples were then submitted to the NUSEQ core.

The single cell library preparation and sequencing was done at Northwestern University NUseq facility core with the support of NIH Grant (1S10OD025120). Cell number and

viability were analyzed using Nexcelom Cellometer Auto2000 with AOPI fluorescent staining method. Sixteen thousand cells were loaded into the Chromium Controller (10X Genomics, PN-120223) on a Chromium Next GEM Chip K (10X Genomics, PN-1000127), and processed to generate single cell gel beads in the emulsion (GEM) according to the manufacturer's protocol. The cDNA and library were generated using the Chromium Next GEM Single Cell 5' Reagent Kits v2 (10X Genomics, PN-1000283) according to the manufacturer's manual. In addition, mouse T-cell and B-cell V(D)J libraries were constructed using Chromium Single cell mouse TCR and BCR Amplification kit (10X Genomics, PN-1000252 and PN-1000255).

The multiplexed libraries were pooled and sequenced on Illumina HiSeq 4000 sequencer with paired-end 50 kits using the following read length: 28 bp Read1 for cell barcode and UMI and 91 bp Read2 for transcript. The targeted sequencing depth for gene expression, mouse T-cell and B-cell V(D)J library is 20000, 5000, and 5000 reads per cell, respectively.

Visualization and Analysis: To visualize the scRNA-seq results obtained, the normalized gene barcode matrix was used to compute a neighborhood graph of cells, then Uniform Manifold Approximation and Projection (UMAP) was performed with default parameters. The whole pipeline was implemented using Scanpy [64]. Cell type annotation was performed using mouse RNA-seq reference and R package SingleR [65]. For validation of human datasets, we also obtained human scRNA-seq data was from 28 GBM cases previously published by Neftel et al., 2019 [66]. All the quality control and filtration parameters as described in the original paper were retained.

Spatial resolved integrated transcriptomics and metabolomics: To obtain the integrative analysis, we used the recently released multi-omics dataset [19] in which Matrix Assisted Laser Desorption/Ionization (MALDI) and array-based spatial transcriptomics (Visium 10X technology) was fully integrated. Downstream analysis and visualization was performed within the SPATA framework using the SPATA2 package (https://github.com/theMILOlab/SPATA2) and the SPATAwrappers (https://github.com/heilandd/SPATAwrappers). Surface plot with H&E images were generated by the function *SPATA2::plotSurface(object, color_by = gene, smooth=T, alpha_by = gene, smooth_span = 0.2)+scale_colour_gradientn(colours = col(50), oob = scales::squish).*

Annotation of cell types and spot-deconvolution was performed by the spaceXR algorithm [67] implemented into SPATAwrappers::runRCTD. For reference, we used the pan-immune single-cell dataset [18]. Single cell plots and analysis was performed by the Seurat package. For spatially weighted correlation analysis, we used the SPATAwrappers:: runSpatialRegression() with the model="CCA" configuration to compare metabolic or transcriptomic features. In the MALDI dataset, target metabolites were obtained by the METASPCAE database (https://metaspace2020.eu).

QUANTIFICATION AND STATISTICAL ANALYSIS

For all ScRNA-seq, spatial transcriptomic and metabolomic analysis, the statistical considerations and quality control information can be found in the original publications. Statistical significance across two groups was determined using two-tailed unpaired

Student's t test performed on figures with individual comparisons. One-way analysis of variance (ANOVA) with Tukey's post hoc was performed for comparisons of three or more groups. Kaplan-Meier curves were generated, and log-rank test was performed to determine significance of in vivo survival rates. P values were calculated in Prism software (GraphPad, San Diego, CA), and the significance is as stated in the figure legends. Error bars are shown as ±SEMs for all figures. For MetaboAnalyst data in Figure 1A, normalized peak areas were input and heatmaps were generated based on t test statistical significance. Methods to assess whether the data met assumptions of the statistical approach, such as tests for normal distribution, were employed when appropriate. All statistics were validated by T.X.

Supplementary Material

Refer to Web version on PubMed Central for supplementary material.

ACKNOWLEDGEMENTS

This work was supported by the Northwestern University RHLCCC Flow Cytometry Facility and a Cancer Center Support Grant (NCI CA060553). We would like to thank Prof. Ben-Sahra (Northwestern) for his assistance in development and analyses of ^{13}C-flux studies. We would also like to thank Isabel Kurth and Inspirna for both RGX-202-01 and continuous advice and guidance on this project. We would also like to thank Ting Xiao who consulted on and verified the statistical analyses in this work. We would also like to thank Cheryl Olson, Alicia Steffens and Katy McCortney for their expertise in immunostaining they performed as part of the Northwestern Nervous System Tumor Bank. This tissue bank is supported by the P50CA221747 SPORE for Translational Approaches to Brain Cancer. Histology services were provided by the Northwestern University Mouse Histology and Phenotyping Laboratory which is supported by NCI P30-CA060553 awarded to the Robert H Lurie Comprehensive Cancer Center.

Funding:

National Institutes of Health / NINDS grant 1R01NS115955-01 (MSL, JM)

National Institutes of Health / NCI grant (JM) - 1R01CA279686-01

National Institutes of Health / NINDS grant P50CA221747 (MSL, JM) SPORE subaward

National Institutes of Health / NCI R35CA197532 (NSC)

National Institutes of Health / R01NS096376-06A1 1R01CA223547-01

References

1. Stupp R, Mason WP, van den Bent MJ, Weller M, Fisher B, Taphoorn MJ, Belanger K, Brandes AA, Marosi C, Bogdahn U, et al. (2005). Radiotherapy plus concomitant and adjuvant temozolomide for glioblastoma. The New England journal of medicine 352, 987–996. 10.1056/NEJMoa043330. [PubMed: 15758009]
2. Akkari L, Bowman RL, Tessier J, Klemm F, Handgraaf SM, de Groot M, Quail DF, Tillard L, Gadiot J, Huse JT, et al. (2020). Dynamic changes in glioma macrophage populations after radiotherapy reveal CSF-1R inhibition as a strategy to overcome resistance. Sci Transl Med 12. 10.1126/scitranslmed.aaw7843.
3. Miska J, Rashidi A, Lee-Chang C, Gao P, Lopez-Rosas A, Zhang P, Burga R, Castro B, Xiao T, Han Y, et al. (2021). Polyamines drive myeloid cell survival by buffering intracellular pH to promote immunosuppression in glioblastoma. Sci Adv 7. 10.1126/sciadv.abc8929.
4. Zhang P, Miska J, Lee-Chang C, Rashidi A, Panek WK, An S, Zannikou M, Lopez-Rosas A, Han Y, Xiao T, et al. (2019). Therapeutic targeting of tumor-associated myeloid cells synergizes with radiation therapy for glioblastoma. Proc Natl Acad Sci U S A 116, 23714–23723. 10.1073/pnas.1906346116. [PubMed: 31712430]

5. Lee-Chang C, Rashidi A, Miska J, Zhang P, Pituch KC, Hou D, Xiao T, Fischietti M, Kang SJ, Appin CL, et al. (2019). Myeloid-derived suppressive cells promote B cell-mediated immunosuppression via transfer of PD-L1 in glioblastoma. Cancer immunology research. 10.1158/2326-6066.CIR-19-0240.
6. Liang H, Deng L, Hou Y, Meng X, Huang X, Rao E, Zheng W, Mauceri H, Mack M, Xu M, et al. (2017). Host STING-dependent MDSC mobilization drives extrinsic radiation resistance. Nat Commun 8, 1736. 10.1038/s41467-017-01566-5. [PubMed: 29170400]
7. Baghdadi M, Wada H, Nakanishi S, Abe H, Han N, Putra WE, Endo D, Watari H, Sakuragi N, Hida Y, et al. (2016). Chemotherapy-Induced IL34 Enhances Immunosuppression by Tumor-Associated Macrophages and Mediates Survival of Chemoresistant Lung Cancer Cells. Cancer Research 76, 6030–6042. 10.1158/0008-5472.Can-16-1170. [PubMed: 27550451]
8. Thorsson V, Gibbs DL, Brown SD, Wolf D, Bortone DS, Yang THO, Porta-Pardo E, Gao GF, Plaisier CL, Eddy JA, et al. (2018). The Immune Landscape of Cancer. Immunity 48, 812–+. 10.1016/j.immuni.2018.03.023. [PubMed: 29628290]
9. Klemm F, Maas RR, Bowman RL, Kornete M, Soukup K, Nassiri S, Brouland JP, Iacobuzio-Donahue CA, Brennan C, Tabar V, et al. (2020). Interrogation of the Microenvironmental Landscape in Brain Tumors Reveals Disease-Specific Alterations of Immune Cells. Cell 181, 1643–1660 e1617. 10.1016/j.cell.2020.05.007. [PubMed: 32470396]
10. Chang AL, Miska J, Wainwright DA, Dey M, Rivetta CV, Yu D, Kanojia D, Pituch KC, Qiao J, Pytel P, et al. (2016). CCL2 Produced by the Glioma Microenvironment Is Essential for the Recruitment of Regulatory T Cells and Myeloid-Derived Suppressor Cells. Cancer Research 76, 5671–5682. 10.1158/0008-5472.Can-16-0144. [PubMed: 27530322]
11. Flores-Toro JA, Luo D, Gopinath A, Sarkisian MR, Campbell JJ, Charo IF, Singh R, Schall TJ, Datta M, Jain RK, et al. (2020). CCR2 inhibition reduces tumor myeloid cells and unmasks a checkpoint inhibitor effect to slow progression of resistant murine gliomas. Proc Natl Acad Sci U S A 117, 1129–1138. 10.1073/pnas.1910856117. [PubMed: 31879345]
12. Otvos B, Silver DJ, Mulkearns-Hubert EE, Alvarado AG, Turaga SM, Sorensen MD, Rayman P, Flavahan WA, Hale JS, Stoltz K, et al. (2016). Cancer Stem Cell-Secreted Macrophage Migration Inhibitory Factor Stimulates Myeloid Derived Suppressor Cell Function and Facilitates Glioblastoma Immune Evasion. Stem Cells 34, 2026–2039. 10.1002/stem.2393. [PubMed: 27145382]
13. Pyonteck SM, Akkari L, Schuhmacher AJ, Bowman RL, Sevenich L, Quail DF, Olson OC, Quick ML, Huse JT, Teijeiro V, et al. (2013). CSF-1R inhibition alters macrophage polarization and blocks glioma progression. Nat Med 19, 1264–1272. 10.1038/nm.3337. [PubMed: 24056773]
14. Quail DF, Bowman RL, Akkari L, Quick ML, Schuhmacher AJ, Huse JT, Holland EC, Sutton JC, and Joyce JA (2016). The tumor microenvironment underlies acquired resistance to CSF-1R inhibition in gliomas. Science 352, aad3018. 10.1126/science.aad3018. [PubMed: 27199435]
15. Brat DJ (2012). Glioblastoma: biology, genetics, and behavior. Am Soc Clin Oncol Educ Book, 102–107. 10.14694/EdBook_AM.2012.32.10210.14694/EdBook_AM.2012.32.48. [PubMed: 24451717]
16. Homma T, Fukushima T, Vaccarella S, Yonekawa Y, Di Patre PL, Franceschi S, and Ohgaki H (2006). Correlation among pathology, genotype, and patient outcomes in glioblastoma. J Neuropath Exp Neur 65, 846–854. DOI 10.1097/01.jnen.0000235118.75182.94. [PubMed: 16957578]
17. Markwell SM, Ross JL, Olson CL, and Brat DJ (2022). Necrotic reshaping of the glioma microenvironment drives disease progression. Acta Neuropathol 143, 291–310. 10.1007/s00401-021-02401-4. [PubMed: 35039931]
18. Ravi VM, Neidert N, Will P, Joseph K, Maier JP, Kuckelhaus J, Vollmer L, Goeldner JM, Behringer SP, Scherer F, et al. (2022). T-cell dysfunction in the glioblastoma microenvironment is mediated by myeloid cells releasing interleukin-10. Nat Commun 13, 925. 10.1038/s41467-022-28523-1. [PubMed: 35177622]
19. Ravi VM, Will P, Kueckelhaus J, Sun N, Joseph K, Salie H, Vollmer L, Kuliesiute U, von Ehr J, Benotmane JK, et al. (2022). Spatially resolved multi-omics deciphers bidirectional tumor-host interdependence in glioblastoma. Cancer Cell 40, 639–655 e613. 10.1016/j.ccell.2022.05.009. [PubMed: 35700707]

20. Bhaduri A, Di Lullo E, Jung D, Muller S, Crouch EE, Espinosa CS, Ozawa T, Alvarado B, Spatazza J, Cadwell CR, et al. (2020). Outer Radial Glia-like Cancer Stem Cells Contribute to Heterogeneity of Glioblastoma. Cell Stem Cell 26, 48–63 e46. 10.1016/j.stem.2019.11.015. [PubMed: 31901251]
21. Brat DJ, Castellano-Sanchez AA, Hunter SB, Pecot M, Cohen C, Hammond EH, Devi SN, Kaur B, and Van Meir EG (2004). Pseudopalisades in glioblastoma are hypoxic, express extracellular matrix proteases, and are formed by an actively migrating cell population. Cancer Res 64, 920–927. 10.1158/0008-5472.can-03-2073. [PubMed: 14871821]
22. Swinson DE, Jones JL, Richardson D, Wykoff C, Turley H, Pastorek J, Taub N, Harris AL, and O'Byrne KJ (2003). Carbonic anhydrase IX expression, a novel surrogate marker of tumor hypoxia, is associated with a poor prognosis in non-small-cell lung cancer. J Clin Oncol 21, 473–482. 10.1200/JCO.2003.11.132. [PubMed: 12560438]
23. Satoh J, Kino Y, Asahina N, Takitani M, Miyoshi J, Ishida T, and Saito Y (2016). TMEM119 marks a subset of microglia in the human brain. Neuropathology 36, 39–49. 10.1111/neup.12235. [PubMed: 26250788]
24. Hambardzumyan D, Amankulor NM, Helmy KY, Becher OJ, and Holland EC (2009). Modeling Adult Gliomas Using RCAS/t-va Technology. Transl Oncol 2, 89–95. 10.1593/tlo.09100. [PubMed: 19412424]
25. Chamberlain KA, Chapey KS, Nanescu SE, and Huang JK (2017). Creatine Enhances Mitochondrial-Mediated Oligodendrocyte Survival After Demyelinating Injury. J Neurosci 37, 1479–1492. 10.1523/JNEUROSCI.1941-16.2016. [PubMed: 28069926]
26. Zhang P, Rashidi A, Zhao J, Silvers C, Wang H, Castro B, Ellingwood A, Han Y, Lopez-Rosas A, Zannikou M, et al. (2023). STING agonist-loaded, CD47/PD-L1-targeting nanoparticles potentiate antitumor immunity and radiotherapy for glioblastoma. Nat Commun 14, 1610. 10.1038/s41467-023-37328-9. [PubMed: 36959214]
27. Sandell LL, Guan XJ, Ingram R, and Tilghman SM (2003). Gatm, a creatine synthesis enzyme, is imprinted in mouse placenta. P Natl Acad Sci USA 100, 4622–4627. 10.1073/pnas.0230424100.
28. Mekhail K, Gunaratnam L, Bonicalzi ME, and Lee S (2004). HIF activation by pH-dependent nucleolar sequestration of VHL. Nat Cell Biol 6, 642–647. 10.1038/ncb1144. [PubMed: 15181450]
29. Vengellur A, Phillips JM, Hogenesch JB, and LaPres JJ (2005). Gene expression profiling of hypoxia signaling in human hepatocellular carcinoma cells. Physiol Genomics 22, 308–318. 10.1152/physiolgenomics.00045.2004. [PubMed: 15942021]
30. Manalo DJ, Rowan A, Lavoie T, Natarajan L, Kelly BD, Ye SQ, Garcia JG, and Semenza GL (2005). Transcriptional regulation of vascular endothelial cell responses to hypoxia by HIF-1. Blood 105, 659–669. 10.1182/blood-2004-07-2958. [PubMed: 15374877]
31. Oudman I, Clark JF, and Brewster LM (2013). The effect of the creatine analogue beta-guanidinopropionic acid on energy metabolism: a systematic review. Plos One 8, e52879. 10.1371/journal.pone.0052879. [PubMed: 23326362]
32. Kurmi K, Hitosugi S, Yu J, Boakye-Agyeman F, Wiese EK, Larson TR, Dai Q, Machida YJ, Lou Z, Wang L, et al. (2018). Tyrosine Phosphorylation of Mitochondrial Creatine Kinase 1 Enhances a Druggable Tumor Energy Shuttle Pathway. Cell Metab 28, 833–847 e838. 10.1016/j.cmet.2018.08.008. [PubMed: 30174304]
33. Kurth I, Andreu C, Takeda S, Tian H, Gonsalves F, Leites K, Sridhar S, Loo JM, Busby R, Tavazoie S, and Tavazoie M (2018). RGX-202, a first-in-class small-molecule inhibitor of the creatine transporter SLC6a8, is a robust suppressor of cancer growth and metastatic progression. Cancer Research 78. 10.1158/1538-7445.Am2018-5863.
34. Kurth I, Yamaguchi N, Andreu-Agullo C, Tian HS, Sridhar S, Takeda S, Gonsalves FC, Loo JM, Barlas A, Manova-Todorova K, et al. (2021). Therapeutic targeting of SLC6A8 creatine transporter suppresses colon cancer progression and modulates human creatine levels. Sci Adv 7, eabi7511. 10.1126/sciadv.abi7511. [PubMed: 34613776]
35. Li Q, Liu M, Sun Y, Jin T, Zhu P, Wan X, Hou Y, and Tu G (2021). SLC6A8-mediated intracellular creatine accumulation enhances hypoxic breast cancer cell survival via ameliorating oxidative stress. J Exp Clin Cancer Res 40, 168. 10.1186/s13046-021-01933-7. [PubMed: 33990217]

36. Lee J, Kotliarova S, Kotliarov Y, Li AG, Su Q, Donin NM, Pastorino S, Purow BW, Christopher N, Zhang W, et al. (2006). Tumor stem cells derived from glioblastomas cultured in bFGF and EGF more closely mirror the phenotype and genotype of primary tumors than do serum-cultured cell lines. Cancer Cell 9, 391–403. 10.1016/j.ccr.2006.03.030. [PubMed: 16697959]
37. Marumoto T, Tashiro A, Friedmann-Morvinski D, Scadeng M, Soda Y, Gage FH, and Verma IM (2009). Development of a novel mouse glioma model using lentiviral vectors. Nat Med 15, 110–116. 10.1038/nm.1863. [PubMed: 19122659]
38. Bendell JC, Strauss JF, Fakih M, McRee AJ, Hendifar AE, Rosen LS, Cercek A, Rowinsky EK, Szarek M, Gonsalves F, et al. (2020). Phase I monotherapy dose escalation of RGX-202, a first-in-class oral inhibitor of the SLC6a8/CKB pathway, in patients with advanced gastrointestinal (GI) solid tumors. J Clin Oncol 38.
39. Kazak L, Chouchani ET, Lu GZ, Jedrychowski MP, Bare CJ, Mina AI, Kumari M, Zhang S, Vuckovic I, Laznik-Bogoslavski D, et al. (2017). Genetic Depletion of Adipocyte Creatine Metabolism Inhibits Diet-Induced Thermogenesis and Drives Obesity. Cell Metab 26, 660–671 e663. 10.1016/j.cmet.2017.08.009. [PubMed: 28844881]
40. Luk GD (1986). Essential role of polyamine metabolism in hepatic regeneration. Inhibition of deoxyribonucleic acid and protein synthesis and tissue regeneration by difluoromethylornithine in the rat. Gastroenterology 90, 1261–1267. 10.1016/0016-5085(86)90394-x. [PubMed: 3082705]
41. Gerner EW, and Meyskens FL Jr. (2004). Polyamines and cancer: old molecules, new understanding. Nat Rev Cancer 4, 781–792. 10.1038/nrc1454. [PubMed: 15510159]
42. Steggerda SM, Bennett MK, Chen JS, Emberley E, Huang T, Janes JR, Li WQ, MacKinnon AL, Makkouk A, Marguier G, et al. (2017). Inhibition of arginase by CB-1158 blocks myeloid cell-mediated immune suppression in the tumor microenvironment. Journal for Immunotherapy of Cancer 5. ARTN 101 10.1186/s40425-017-0308-4. [PubMed: 29254508]
43. Heiland DH, Gaebelein A, Borries M, Worner J, Pompe N, Franco P, Heynckes S, Bartholomae M, hAilin DO, Carro MS, et al. (2018). Microenvironment-Derived Regulation of HIF Signaling Drives Transcriptional Heterogeneity in Glioblastoma Multiforme. Molecular cancer research : MCR 16, 655–668. 10.1158/1541-7786.MCR-17-0680. [PubMed: 29330292]
44. Salomons GS, van Dooren SJ, Verhoeven NM, Cecil KM, Ball WS, Degrauw TJ, and Jakobs C (2001). X-linked creatine-transporter gene (SLC6A8) defect: a new creatine-deficiency syndrome. Am J Hum Genet 68, 1497–1500. 10.1086/320595. [PubMed: 11326334]
45. Zhu S, Li M, Figueroa BE, Liu A, Stavrovskaya IG, Pasinelli P, Beal MF, Brown RH Jr., Kristal BS, Ferrante RJ, and Friedlander RM (2004). Prophylactic creatine administration mediates neuroprotection in cerebral ischemia in mice. J Neurosci 24, 5909–5912. 10.1523/JNEUROSCI.1278-04.2004. [PubMed: 15229238]
46. Prass K, Royl G, Lindauer U, Freyer D, Megow D, Dirnagl U, Stockler-Ipsiroglu G, Wallimann T, and Priller J (2007). Improved reperfusion and neuroprotection by creatine in a mouse model of stroke. J Cereb Blood Flow Metab 27, 452–459. 10.1038/sj.jcbfm.9600351. [PubMed: 16773141]
47. Beal MF (2011). Neuroprotective effects of creatine. Amino Acids 40, 1305–1313. 10.1007/s00726-011-0851-0. [PubMed: 21448659]
48. Brosnan JT, da Silva RP, and Brosnan ME (2011). The metabolic burden of creatine synthesis. Amino Acids 40, 1325–1331. 10.1007/s00726-011-0853-y. [PubMed: 21387089]
49. Horska A, and Barker PB (2010). Imaging of brain tumors: MR spectroscopy and metabolic imaging. Neuroimaging Clin N Am 20, 293–310. 10.1016/j.nic.2010.04.003. [PubMed: 20708548]
50. Kinoshita Y, and Yokota A (1997). Absolute concentrations of metabolites in human brain tumors using in vitro proton magnetic resonance spectroscopy. NMR Biomed 10, 2–12. 10.1002/(sici)1099-1492(199701)10:1<2::aid-nbm442>3.0.co;2-n. [PubMed: 9251109]
51. Nguyen ML, Willows B, Khan R, Chi A, Kim L, Nour SG, Sroka T, Kerr C, Godinez J, Mills M, et al. (2014). The potential role of magnetic resonance spectroscopy in image-guided radiotherapy. Front Oncol 4, 91. 10.3389/fonc.2014.00091. [PubMed: 24847443]
52. Delorme S, and Weber MA (2006). Applications of MRS in the evaluation of focal malignant brain lesions. Cancer Imaging 6, 95–99. 10.1102/1470-7330.2006.0015. [PubMed: 16829470]

53. Sondergaard KL, Hilton DA, Penney M, Ollerenshaw M, and Demaine AG (2002). Expression of hypoxia-inducible factor 1alpha in tumours of patients with glioblastoma. Neuropathol Appl Neurobiol 28, 210–217. [PubMed: 12060345]
54. Hambardzumyan D, and Bergers G (2015). Glioblastoma: Defining Tumor Niches. Trends Cancer 1, 252–265. 10.1016/j.trecan.2015.10.009. [PubMed: 27088132]
55. Barker FG, Davis RL, Chang SM, and Prados MD (1996). Necrosis as a prognostic factor in glioblastoma multiforme. Cancer 77, 1161–1166. Doi 10.1002/(Sici)1097-0142(19960315)77:6<1161::Aid-Cncr24>3.0.Co;2-Z. [PubMed: 8635139]
56. Di Biase S, Ma X, Wang X, Yu J, Wang YC, Smith DJ, Zhou Y, Li Z, Kim YJ, Clarke N, et al. (2019). Creatine uptake regulates CD8 T cell antitumor immunity. The Journal of experimental medicine 216, 2869–2882. 10.1084/jem.20182044. [PubMed: 31628186]
57. Samborska B, Roy DG, Rahbani JF, Hussain MF, Ma EH, Jones RG, and Kazak L (2022). Creatine transport and creatine kinase activity is required for CD8(+) T cell immunity. Cell Rep 38, 110446. 10.1016/j.celrep.2022.110446. [PubMed: 35235777]
58. Darabedian N, Ji W, Fan M, Lin S, Seo HS, Vinogradova EV, Yaron TM, Mills EL, Xiao H, Senkane K, et al. (2023). Depletion of creatine phosphagen energetics with a covalent creatine kinase inhibitor. Nat Chem Biol. 10.1038/s41589-023-01273-x.
59. Billingham LK, Stoolman JS, Vasan K, Rodriguez AE, Poor TA, Szibor M, Jacobs HT, Reczek CR, Rashidi A, Zhang P, et al. (2022). Mitochondrial electron transport chain is necessary for NLRP3 inflammasome activation. Nat Immunol. 10.1038/s41590-022-01185-3.
60. Tachikawa M, and Hosoya K (2011). Transport characteristics of guanidino compounds at the blood-brain barrier and blood-cerebrospinal fluid barrier: relevance to neural disorders. Fluids Barriers CNS 8, 13. 10.1186/2045-8118-8-13. [PubMed: 21352605]
61. Spencer D, Yu D, Morshed RA, Li G, Pituch KC, Gao DX, Bertolino N, Procissi D, Lesniak MS, and Balyasnikova IV (2019). Pharmacologic modulation of nasal epithelium augments neural stem cell targeting of glioblastoma. Theranostics 9, 2071–2083. 10.7150/thno.29581. [PubMed: 31037157]
62. Miska J, Rashidi A, Chang AL, Muroski ME, Han Y, Zhang L, and Lesniak MS (2016). Anti-GITR therapy promotes immunity against malignant glioma in a murine model. Cancer immunology, immunotherapy : CII 65, 1555–1567. 10.1007/s00262-016-1912-8.
63. Sanjana NE, Shalem O, and Zhang F (2014). Improved vectors and genome-wide libraries for CRISPR screening. Nat Methods 11, 783–784. 10.1038/nmeth.3047. [PubMed: 25075903]
64. Wolf FA, Angerer P, and Theis FJ (2018). SCANPY: large-scale single-cell gene expression data analysis. Genome Biol 19, 15. 10.1186/s13059-017-1382-0. [PubMed: 29409532]
65. Aran D, Looney AP, Liu L, Wu E, Fong V, Hsu A, Chak S, Naikawadi RP, Wolters PJ, Abate AR, et al. (2019). Reference-based analysis of lung single-cell sequencing reveals a transitional profibrotic macrophage. Nat Immunol 20, 163–172. 10.1038/s41590-018-0276-y. [PubMed: 30643263]
66. Neftel C, Laffy J, Filbin MG, Hara T, Shore ME, Rahme GJ, Richman AR, Silverbush D, Shaw ML, Hebert CM, et al. (2019). An Integrative Model of Cellular States, Plasticity, and Genetics for Glioblastoma. Cell 178, 835–849 e821. 10.1016/j.cell.2019.06.024. [PubMed: 31327527]
67. Cable DM, Murray E, Shanmugam V, Zhang S, Zou LS, Diao M, Chen H, Macosko EZ, Irizarry RA, and Chen F (2022). Cell type-specific inference of differential expression in spatial transcriptomics. Nat Methods. 10.1038/s41592-022-01575-3.

Highlights

- Myeloid cells in the hypoxic niche of GBM upregulate *de novo* creatine biosynthesis
- TAMC-generated creatine is taken up by GBM cells under hypoxic stress
- Creatine uptake by GBM tissue supports its growth, survival, and stem-cell phenotypes
- Inhibition of creatine uptake presents a potential therapeutic strategy for GBM

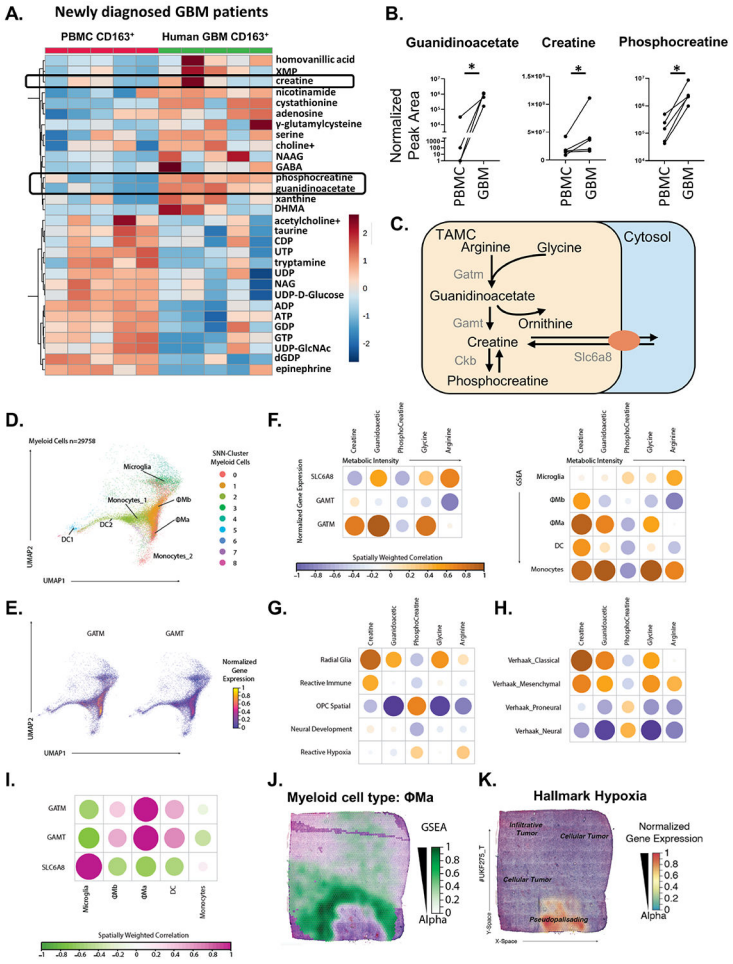

Fig. 1: Tumor-associated myeloid cells (TAMC) produce creatine *de-novo* from arginine.

In (**A-B**), Five matched tumor and PBMC samples were obtained from patients with newly diagnosed GBM, and CD163^{+} magnetic bead-based isolation was performed prior to running untargeted metabolomics via LC-MS. In (**A**), a heat-map of changes in peripheral versus tumoral myeloid cells organized by paired t-test significance (top 25 shown), and in (**B**), normalized peak area measurements of key creatine metabolites in the five matched samples. In (**C**), schema of the *de-novo* creatine biosynthetic pathway. In (**D**) dimensional reduction of myeloid cells in human GBM [18]. Colors indicate the cluster affiliation based on an iterative shared nearest neighbor approach and the indicated cell types are based on the classification of Ravi et al. In (**E**), dimensional reduction with gene expression of *GATM* and *GAMT* indicating an enhanced expression in the activated myeloid cluster. In (**F**), spatially weighted correlation analysis of the integrated spatially resolved transcriptomic-metabolomic dataset [19], performed for the GATM, GAMT and SCL6A8 genes (*left panel*), the myeloid cell types (*right panel*). In (**G**) the spatially distinct transcriptional phenotypes, and in (**H**) the Verhaak subgroups. In (**I**) the comparison and validation of *GAMT, GATM* and *SCL6A8* expression with its spatially weighted correlation to the myeloid cell types. In (**J**), the spatial localization of the ΘMa population surrounding the hypoxic and pseudopalisading niche. In (**K**), normalized spatial gene expression for hallmark hypoxia

genes overlaid with paired H&E image. In **A-B**, n=5 paired PBMC and tumor samples with statistics via calculated paired Student's t-test. Data in **D-K** is pooled and analyzed from 16 patients with GBM. *=p<0.05; **=p<0.01; ***=p<0.001.

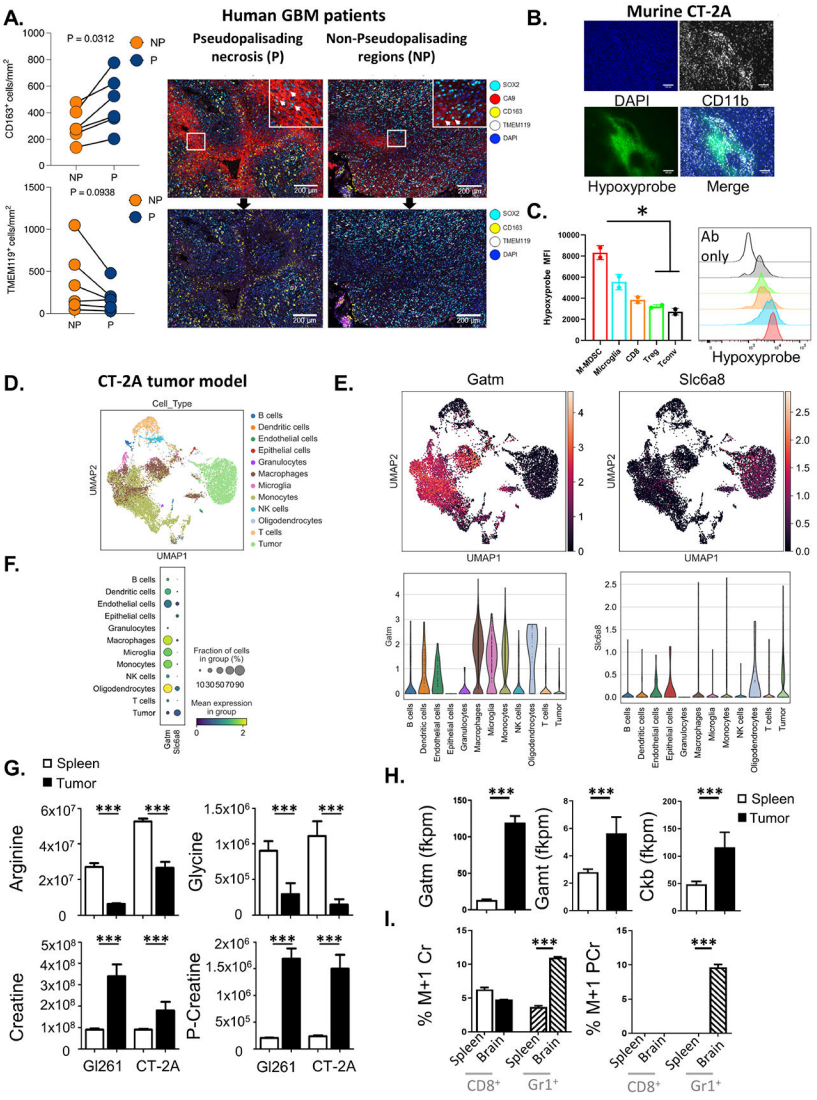

Fig. 2: Creatine synthesis and uptake is both spatially and cellularly compartmentalized in the hypoxic niche.

In (**A**), multiplexed immunofluorescence to examine the location of macrophages ($CD163^+$) or microglia (TMEM119) in the context of hypoxic regions surrounding necrosis. In (**B**), immunostaining of flash frozen tumors and (**C**), MFI of hydroxyprobe in M-MDSCs, microglia, CD8, Tregs, and Tconv from mice implanted intracranially (i.c.) with CT-2A tumors for 14 days and injected i.v. with pimonidazole. In (**D-F**), single R annotation of all major cell populations from scRNA-sequencng of $CD45^+$ cells isolated from CT-2A tumors 2 weeks post i.c. implantation. In (**G**), bulk metabolomic analysis of splenic macrophage and TAMC populations isolated 2 weeks post i.c. with GL261 or CT-2A tumor cells. In (**H**), FKPM values of all genes involved in *de-novo* creatine biosynthesis from our previously published dataset [3]. In (**I**), percent M+1 creatine in splenic $CD8^+$ T-cell and TAMC populations cultured with ^{13}C-arginine overnight. Significance was calculated via a paired Student's t-test in **A**, and unpaired Student's t-test in **H** In **A,** n=6 GBM tissues with the entire section analyzed. In **D-F,** n= 2-3 independent experiments with n=5-10 tumors

pooled per n. Data shown in **G-I** is integrated from two independent experiments. Error bars are expressed as mean ± SEM. p<0.05*, p<0.01**, p<0.001***.

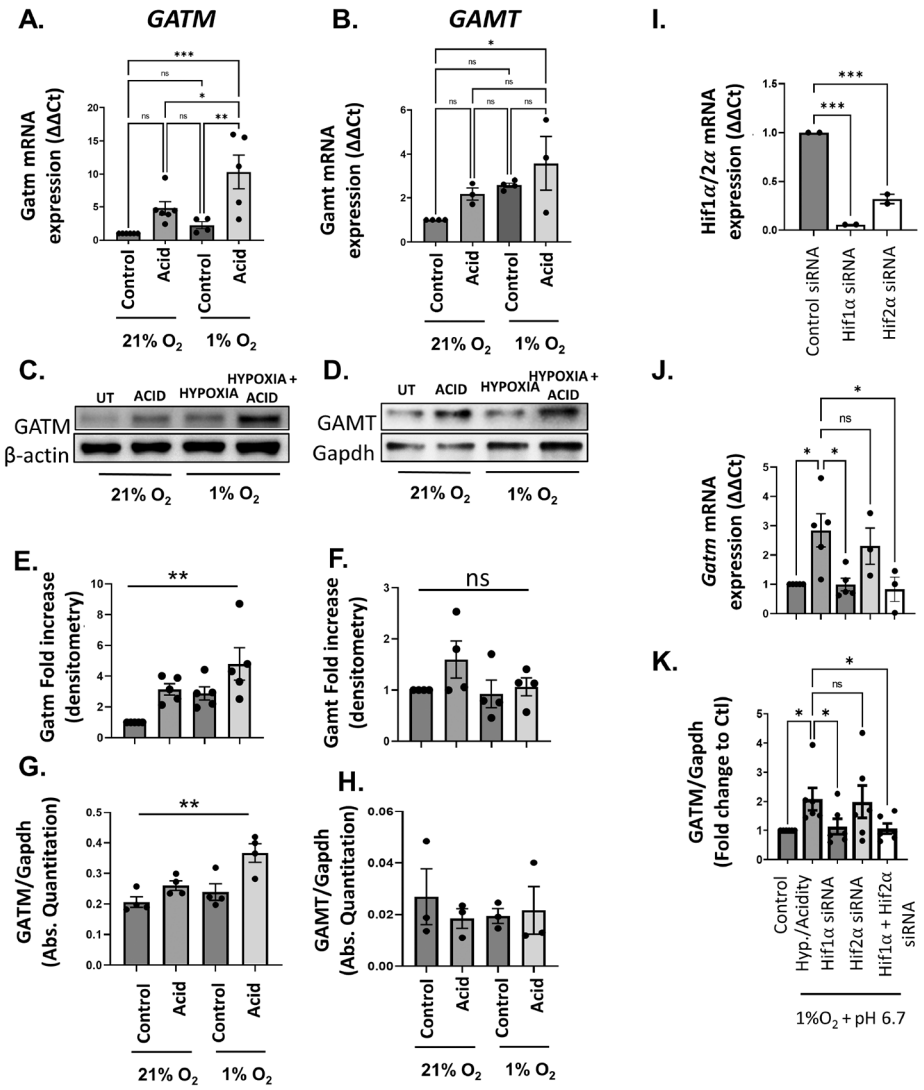

Fig. 3. *De-novo* Creatine synthesis is regulated by HIF1*a* in TAMCs.

In (**A-B**) GATM and GAMT mRNA and (**C**) protein expression of *in vitro* generated TAMCs cultured under the indicated conditions for 6h (**A-B**) or 24h (**C-D, G-H**). In (**E-F**), densitometry for **(C**). In (**G-H**), protein expression of GATM (**G**) or GAMT (**H**) normalized to GAPDH under indicated conditions and measured using Protein Simple Wes quantitative western blotting. In (**I**) Hif1*a* and Hif2*a* mRNA expression in TAMCs treated with lipid-nanoparticle (LNP) containing siRNA against murine Hif1*a* or Hif2*a* for 24h. In (**J-K**), GATM mRNA (**J**) and protein (**K**) expression in TAMCs treated with siRNA-containing LNP and subjected to indicated conditions for 6h (**J**) or 24h (**K**). In **A-F,** n=4-6, In **G-H,** n=3-4, in **I,** n=2, and in **J-K,** n=3-6 independent experiments. One Way ANOVA with Tukey's post-hoc was used for all statistical analysis and individual comparisons. Error bars are expressed as mean ± SEM. p<0.05*, p<0.01**, p<0.001***.

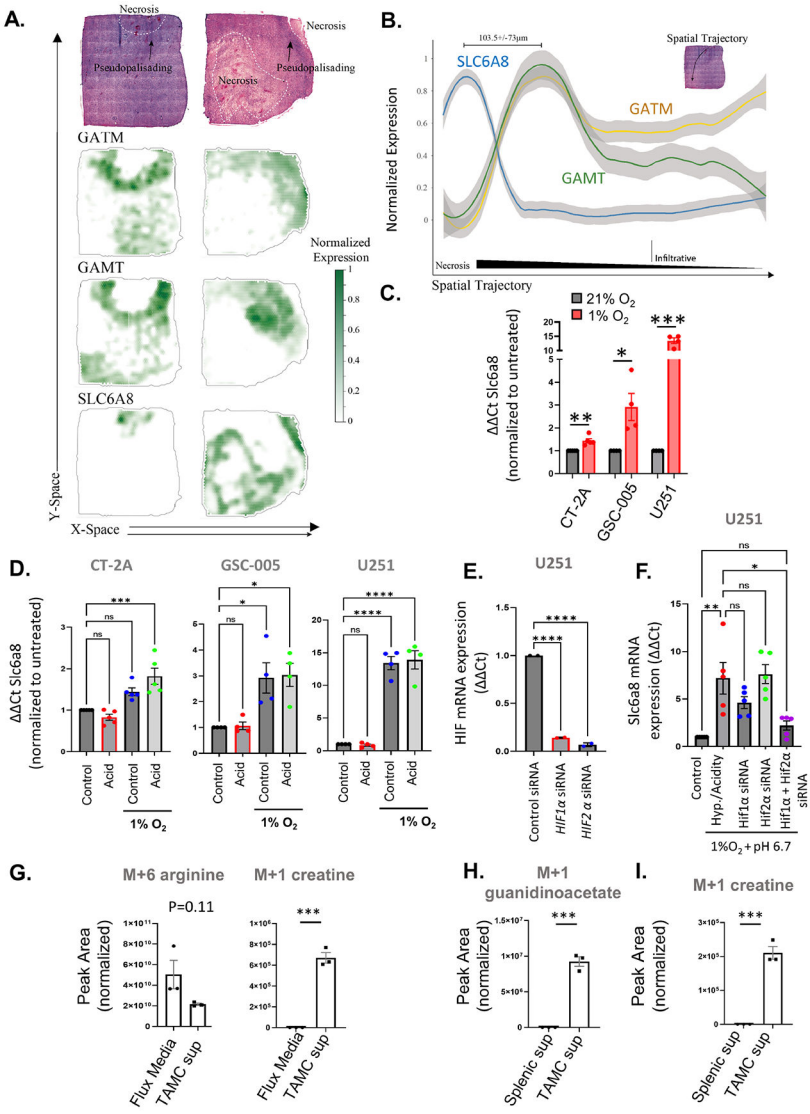

Figure 4. Creatine uptake by GBM is regulated by hypoxia.

In (**A**), two representative images of the spatially weighted gene expression of *GATM, GAMT* and *SLC6A8* in human GBM tissue. In (**B**) spatial trajectory analysis of *SLC6A8*, *GATM* and *GAMT* in relationship to the necrotic niche. In (**C**), *Slc6a8* expression in CT-2A, GSC-005 and U251 tumor cells after 24hrs of 1% O_2. In (**D**) *SLC6A8* upregulation in CT-2A, GSC-005, and U251 GBM cell lines under the indicated conditions for 24 hrs. All experiments in (**D**), are the results of 3-4 independent experiments. In (**E**), HIF mRNA expression in U251 GBM cells treated with LNP-siRNA against HIF1α and HIF2α for 24 hours. In (**F**), *SLC6A8* mRNA expression in U251 cells treated with siRNA-containing LNPs for 24h prior to indicated treatment for 24h. In (**G**), the same siRNAs were used on U251 for 24 hours before being placed under normoxia or hypoxia + acidity (1% O_2 + pHe 6.7) for 24 hours for qPCR analysis. In (**G-I**), 14 days after CT-2A tumor implantation, TAMC and splenic myeloid cells were harvested via magnetic bead isolation and cultured for 24 hours in ^{13}C-arginine media. In (**G**), flux media versus *in-vitro* generated

TAMC supernatant after 24 hours culture in flux media. In (**H-I**), Cell-free supernatant was harvested from splenic or tumor myeloid cells after 24 hours of culture of flux media, and abundance of M+1 Guanidinoacetate (**H**), and M+1 Creatine (**I**) was analyzed via LC-MS. n=2 mice in each group for validation in **E**, N=3-6 mice for qPCR in **C,D,F**. In **G-I**, n=3 replicates representative of two individual experiments. One Way ANOVA with Tukey's post-hoc was used for all statistical analysis in **D-F** and unpaired Student's t-test was used in **C, G-I** to test for significance. Error bars are expressed as mean ± SEM. $p<0.05$*, $p<0.01$**, $p<0.001$***.

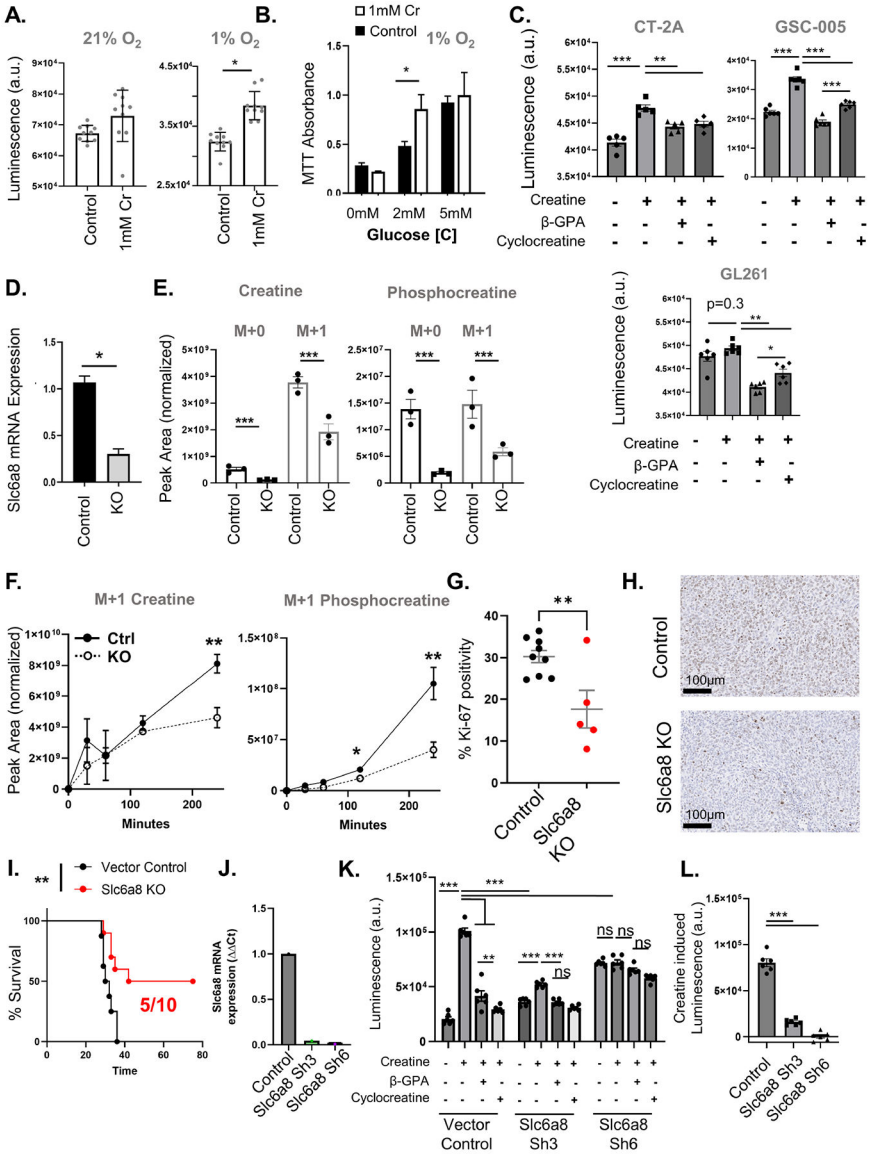

Figure 5. Creatine uptake via SLC6A8 by tumor cells promotes cell growth, viability, and tumor progression.

In (**A**), ATP Luminescence assay in CT-2A tumor cells were cultured in 21% or 1% O_2 hypoxia for 4 hours. In (**B**), MTT assay assessing the viability of CT-2A under hypoxia and reducing concentrations of glucose. In (**C**) cell-titer glo analysis of CT-2A (*left panel*), GSC-005 (*right panel*), or GL261(*bottom panel)* tumor cells under hypoxia/glucose restriction (1mM) given equimolar (1mM) creatine, Creatine + β -GPA, or Creatine + Cyclocreatine for 24 hrs. In (**D**) Slc6a8 mRNA expression in CT-2A tumor cells treated with CRISPR against SLC6A8. In (**E**), the amount of unlabeled and ^{13}C-labelled Creatine after 4 hours of culture in vector control (Vc) and SLC6A8 KO tumor cell lines. In (**F**), the kinetics of M+1 labeled Creatine (Cr) and M+1 labelled phosphocreatine (PCr) over time in control and KO tumor cell lines. In (**G-I**), 7.5x10^4 of Vc and SLC6A8KO CT-2A were implanted orthotopically into WT mice and one cohort of mice was euthanized for Ki-67 immunostaining (**G,H**), and another was monitored for survival and plotted in a Kaplan

Meier curve (**I**). In (**J**) SLC6A8 expression in U251 tumor cell lines treated with shRNA targeting SLC6A8 (and non-targeting controls). In (**K**) and Cell titer Glo luminescence assays in U251 tumor cell lines treated as in (**J**). In (**L**), Cell titer Glo luminescence assay in U251 tumor cells treated with 1mM Creatine. In **A**, n=10 per group; In **B**, n=4-6 per group; in **C**, n=6 per group; in **D-E,** n=3 per group. In **G-I**, n= 9 for Vc tumors, and n=5 for Slc6a8 KO tumors; In **J**, n=1 per group; In **K-L**, n=6 per group. A one Way ANOVA with Tukey's post-hoc was used for all statistical analysis in (**C,E,K,L**) a unpaired Student's t-test was used in (**A,B,D,G**). In **F**, a two-way ANOVA was performed followed by Sidak's multiple comparisons test for significance. In (**I**) Log-Rank analysis was performed. Error bars are expressed as mean ± SEM. $p<0.05$*, $p<0.01$**, $p<0.001$***.

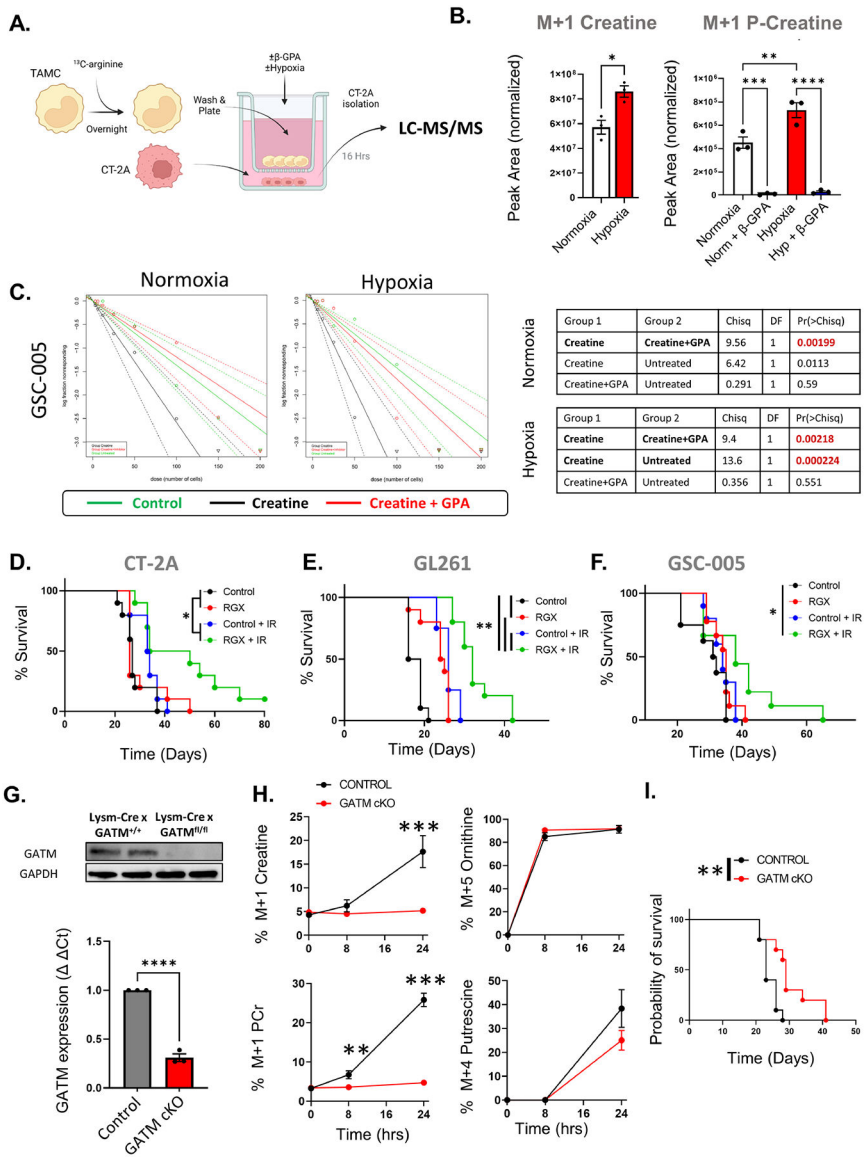

Fig. 6: Inhibition of creatine transport perturbs multiple aspects of GBM biology.

In (**A**), a schematic demonstrating the assay performed in (**B**). In (**B**), Peak area of M+1 creatine (left) and M+1 phospo-creatine (right) in CT-2A tumor cells plated as shown in (**A**) and incubated for 8 hours in normoxia, 1% O_2 hypoxia, +/− 5mM β-GPA. In **(C)** Extreme Limiting Dilution Analysis (ELDA) of GSC-005 neurospheres with a diameter greater than 200mm treated either with 1mM Creatine in the presence or absence of equimolar SLC6A8 inhibitor, 3-Guanidinopropionic acid for 7-10 days. After 7 – 10 days, neurospheres with a diameter greater than 200 μm was counted. In (**D-F**) Kaplan Meier curves of mice implanted with i.c. with $7.5x10^4$ CT-2A, $1x10^5$ GL261 cells, or $5x10^4$ GSC-005 cells (respectively) and administered RGX-202-01 chow and/or 3Gy/3day (9Gy total radiation) or the combination, 7 days post-implantation. In (**G**), western blot (top) or qPCR (bottom) of GATM in TAMC generated *in-vitro* from Ctrl or GATM KO mice. In (**H**), ^{13}C-arginine flux on control and GATM KO *in-vitro* generated TAMCs over 24

hours. In (**I**), Kaplan Meier curve Control vs *Gatm*-cKO mice implanted with $100x10^5$ CT-2A tumor cells. In **B**, n=3-4 per group, representative of two independent experiments. In **C**, n=2 independent experiments. In **D-F** and **I**, n=10 per group (equal gendered), were analyzed. In **G**, n=2 independent experiments performed in duplicate. In **H**, n=3 per group, representative of two independent experiments. In **B** (*left panel*)**,** an unpaired Student's t-test was performed. In **H**, a two-way ANOVA was performed followed by Sidak's multiple comparisons test for significance. In **B** (*right panel)* a one-way ANOVA followed by Tukey's post hoc was performed for significance. In **D-F** and **I**, Log-Rank analysis was performed. In **C,** Statistics calculated used Walter & Eliza Hall Institute of Medical Research platform (https://bioinf.wehi.edu.au/software/elda/). Error bars are expressed as mean ± SEM. $p<0.05$*, $p<0.01$**, $p<0.001$***.

KEY RESOURCES TABLE

REAGENT or RESOURCE	SOURCE	IDENTIFIER
Antibodies		
Mouse Anti-CD206	Biorad	RRID:AB_493697
Human Anti-CD163 Biotin	Biolegend	RRID:AB_1134004
Mouse Anti-CD45 Biotin	Biolegend	RRID:AB_312968
Anti-CD11b Alexa 647	Biolegend	RRID:AB_389327
Human TruStain FcX™	Biolegend	Cat: 422301
Mouse Anti-CD16/32	Biolegend	RRID:AB_312800
Mouse Anti-CD45 BV510	Biolegend	RRID:AB_2561392
Mouse Anti-CD3 PE-Cy7	Biolegend	RRID:AB_1732068
Mouse Anti-C11b BV711	Biolegend	RRID:AB_11218791
Mouse Anti-Ly6C Alexa-Fluor 700	BD Biosciences	RRID:AB_10612017
Mouse Anti-Ly6G Percp–cy5.5	Biolegend	RRID:AB_1877272
Mouse Anti-CD4 BUV395	BD Biosciences	RRID:AB_2739427
Mouse Anti-CD8–BV605	Biolegend	RRID:AB_2561352
Anti-pimonidazole GFP	Hypoxyprobe	HP6-1000Kit
Mouse Anti-Foxp3 Efluor 450	Fisher	RRID:AB_1518812
Human Anti-TMEM119 OPAL 520	Millipore Sigma	RRID:AB_2681645
Human Anti-Sox2 OPAL 620	Abcam	RRID:AB_10585428
Human Anti-CA9 OPAL 540	Novus Biologics	RRID:AB_11011250
Human Anti CD163 OPAL 520	Abcam	RRID:AB_2753196
Bacterial and Virus Strains		
Biological Samples		
lentiCRISPR v2	Addgene	RRID:Addgene_52961
Chemicals, Peptides, and Recombinant Proteins		
RGX-202-01 compound	Inspirna	N/A
L-ARGININE:HCL (13C6, 99%)	Cambridge isotope	CLM-2265-H-PK
1C13 labeled creatine (guanidino group)	Cambridge isotope	CLM-7933-PK
Dialyzed FBS	Fisher	A3382001
SILAC RPMI 1640 Flex Media, no glucose, no phenol red	Fisher	A2494201
DMEM, no Glucose, phenol, glutamine, pyruvate	Fisher	A1443001
Recombinant M-CSF	Peprotech	315-02
Streptavidin MicroBeads	Miltenyi	130-048-101
DMEM/F12	Fisher	11320033

REAGENT or RESOURCE	SOURCE	IDENTIFIER
Recombinant murine EGF	R&D	2028-EG-200
Recombinant murine FGF	R&D	3139-FB-025
B27 supplement	Fisher	17504044
Culture-Insert 2 Well in μ-Dish 35 mm	Ibidi	81176
Pimonidazole	Hypoxyprobe	HP6-1000Kit
Live/Dead Elfuor780	Fisher	65-0865-14
StemPro™ Accutase™ Cell Dissociation Reagent	Fisher	A1110501
Critical Commercial Assays		
CellTiter-Glo® Luminescent Cell Viability Assay	Promega	G7570
Adult Brain Dissociation Kit	Miltenyi	130-107-677
CyQUANT™ MTT Cell Viability Assay	Fisher	V13154
RNeasy Plus Micro Kit	Qiagen	74034
Deposited Data		
Raw and Analyzed data (that is not included in Data S1)	Upon Request	
Raw data/gels/Wes data used to generate figures	Data S1	
Metabolomics Datasets	Metabolomics Workbench	doi: 10.21228/M8PH9P Study: ST002935
Murine scRNA seq data	Biosample submission portal/NIH	BioProject ID: PRJNA1029174
Experimental Models: Cell Lines		
Murine glioma GL-261 Sex: M	NCI	DTP, DCTD TUMOR REPOSITORY RRID:CVCL_Y003
Murine glioma CT-2A Sex: M	Millipore	RRID:CVCL_ZJ44
Murine Glioma: GSC-005 Sex: Unknown	Verma Laboratory	N/A
Human GBM cell line: U251 Sex: M	ATCC	RRID:CVCL_0021
Human GBM PDX: GBM39 Sex: Unknown	James Laboratory	N/A
Experimental Models: Organisms/Strains		
MOUSE: C57 Bl/6	Jackson	Cat#000664; RRID:IMSR_JAX:000664
MOUSE: LysM^{-CRE}	Jackson	RRID:IMSR_JAX:004781
MOUSE: GATM-^{Flox}	Spiegelman Laboratory	N/A
MOUSE: LysM^{-CRE} x GATM-^{Flox}	This Paper	N/A
Oligonucleotides		
β-Actin Forward: TTGCTGACAGGATGCAGAAG	Purchased: IDT	Design: ncbi.nlm.nih.gov/tools/primer-blast/
β-Actin Reverse: ACATCTGCTGGAAGGTGGAC	Purchased: IDT	Design: ncbi.nlm.nih.gov/tools/primer-blast/
Slc6a8 Forward: AGACTTGGACACGCCAGATG	Purchased: IDT	Design: ncbi.nlm.nih.gov/tools/primer-blast/

REAGENT or RESOURCE	SOURCE	IDENTIFIER
Slc6a8 Reverse: TTCCTCCAACCAGGGCAATC	Purchased: IDT	Design: ncbi.nlm.nih.gov/tools/primer-blast/
Mouse Hif1a Forward: CTATGGAGGCCAGAAGAGGGTAT	Purchased: IDT	PMID: 22930750
Mouse Hif1a Reverse: CCCACATCAGGTGGCTCATAA	Purchased: IDT	PMID: 22930750
Mouse Hif2a Forward: CTGAGGAAGGAGAAATCCCGT	Purchased: IDT	PMID: 22930750
Mouse Hif2a Reverse: TGTGTCCGAAGGAAGCTGATG	Purchased: IDT	PMID: 22930750
Human Hif1a Forward: CATAAAGTCTGCAACATGGAAGGT	Purchased: IDT	PMID: 18393939
Human Hif1a Reverse: ATTTGATGGGTGAGGAATGGGTT	Purchased: IDT	PMID: 18393939
Human Hif2a Forward: GCGCTAGACTCCGAGAACAT	Purchased: IDT	PMID: 18393939
Human Hif2a Reverse: TGGCCACTTACTACCTGACCCTT	Purchased: IDT	PMID: 18393939
Slc6a8 Reverse: TTCCTCCAACCAGGGCAATC	Purchased: IDT	Design: ncbi.nlm.nih.gov/tools/primer-blast/
Gatm Forward: GCTTCCTCCCGAAATTCCTGT	Purchased: IDT	Design: ncbi.nlm.nih.gov/tools/primer-blast/
Gatm Reverse: CCTCTAAAGGGTCCCATTCGT	Purchased: IDT	Design: ncbi.nlm.nih.gov/tools/primer-blast/
SiRNA oligos (full list in Data S1)	Purchased: Sigma	
Recombinant DNA		
Software and Algorithms		
Prism	Graphpad	www.graphpad.com; RRID:SCR_002798
Facs Diva	BD	www.bdbiosciences.com
Excel	Microsoft	www.microsoft.com; RRID:SCR_016137
FlowJo	Treestar	www.flowjo.com; RRID:SCR_008520
ImageJ	NIH	imagej.nih.gov/ij/; RRID:SCR_003070
Other		